Mon. Not. R. Astron. Soc. **294,** 201–223 (1998)

The nature of the cometary knots in the Helix planetary nebula (NGC 7293)

J. Meaburn,[1] C. A. Clayton,[2] M. Bryce,[1] J. R. Walsh,[3] A. J. Holloway[1] and W. Steffen[1]

[1]*Department of Physics and Astronomy, University of Manchester, Oxford Road, Manchester M13 9PL*
[2]*Rutherford Appleton Laboratory, Chilton, Didcot, Oxon OX11 0QX*
[3]*Space Telescope Coordinating Facility, ESO, Karl-Schwarzschild-Strasse 2, D-85748 Garching bei München, Germany*

Accepted 1997 August 8. Received 1997 July 30; in original form 1997 May 6

ABSTRACT

The system of cometary knots in the Helix planetary nebula (NGC 7293) has been systematically observed using ground-based images and long-slit, high-resolution spectroscopy. CCD images in the [N II] 6584-Å line, taken with the ESO NTT, are used to determine the spatial distribution of the knots; images in the [O III] 5007-Å line distinguish their position within the nebula on the basis of the absorption of the central [O III] 5007-Å-emitting zone of the Helix nebula. The kinematics of 50 of the brighter knots and their tails were studied primarily with the Manchester Echelle Spectrograph (MES) as well as the ESO NTT using the EMMI spectrograph. Three regions were covered by multiple exposures of a 10-element multislit with MES to obtain [N II] 6584-Å line profiles along 300 individual slit positions. In addition, many long-slit MES spectra, placed diametrically across the nebula, were obtained to compare the kinematics of the knots with the large-scale kinematical structure of the nebula.

The global expansion of the system of knots is around 14 km s^{-1}, some 17 km s^{-1} less than for the overrunning gas, and they are distributed in a thick central disc. The velocity field of the system of knots is similar to that of molecular (CO) emission but with a lower expansion velocity. Most knots are external to the central [O III] 5007-Å-emitting region, but some still show localized [O III] 5007-Å emission from their heads.

The kinematical structure of two of the latter knots as revealed by profiles of the [O I] 6300-Å, [N II] 6584-Å, [O III] 5007-Å and Hα emission lines is considered in detail and compared with their CO emission-line profiles. The interstellar absorption by the core of a further knot is derived from an [O III] 5007-Å *HST* image combined with MES [O III] 5007-Å profiles. Accurate masses, densities and ages are determined as a consequence. Furthermore, a kinematical model shows that the [N II] 6584-Å-emitting flow around a dusty, molecular globule (the core of an ionized knot) arises mainly from the expanding ionized gas of the Helix nebula engulfing the knot. The flow, parallel to the globule's photoionized surface, is mildly supersonic. The relationship between the system of knots and the large-scale structure is discussed.

Key words: planetary nebulae: individual: NGC 7293.

1 INTRODUCTION

The Helix nebula, NGC 7293, is unique amongst planetary nebulae (PNe) in that, at a distance of 130 pc (Cahn & Kaler 1971; Acker 1978; Daub 1982, although Cahn, Kaler & Stanghellini 1992 have now revised their estimate to 160 pc), it is the only PN in which small-scale structure can easily be seen with ground-based instruments and examined in detail with the *HST*. Indeed, the Helix nebula is the only PN in which ionized knots with comet-like

© 1998 RAS

tails have been observed (by Baade and reported by Verontsov-Velyaminov 1968). However, there is no reason to conclude that the Helix nebula is unique in this respect, and it is probable that such knots may exist in the majority of PNe but are not detectable from ground-based observations.

These knots show a number of interesting features. First, the ionized knots themselves exhibit crescent-shaped heads, the apices of which point towards the central star. The ionized crescents are therefore partial skins on the surfaces of dense ($\approx 10^6\,\mathrm{cm}^{-3}$), dusty, molecular globules. This structure was reported after optical observations by Meaburn et al. (1992) and millimetre CO observations by Huggins et al. (1992), and subsequently seen in detail in spectacular *HST* images (O'Dell & Handron 1996). Secondly, the cometary tails all point radially away from the central star, which has an effective temperature of 120 000 K (Bohlin, Harrington & Stecher 1982) and is responsible for making the Helix nebula a typical high-ionization PN with emission lines of He II and higher ionization species from the vicinity of its core, i.e., the central cavity is a high-ionization region, in contrast to the outer rings which consist of low-ionization material (Warner & Rubin 1975). Incidentally, the observations of the very narrow CO line profiles (1–2 km s^{-1} HPBW) from the globule cores (Huggins et al. 1992) are relevant to the interpretation of the widths of the complementary optical line profiles to be considered later in the present paper.

The Helix nebula itself has a complex structure. It gains its name from its large-scale helical appearance when viewed in the light of low-ionization species such as [N II] 6584 Å. In high-ionization emission (e.g., [O III] 5007 Å), a central, nearly spherical structure is observed instead (Meaburn & White 1982). Substantial amounts of cool molecular gas (perhaps in the form of dense, shielded clumps) can be inferred from the extensive CO (Huggins & Healy 1986; Forveille & Huggins 1991; Huggins et al. 1992; Young et al. 1997) and H_2 (Storey 1984; Kastner et al. 1996) emission that is observed to be coincident with the helical structure. Many attempts have been made to understand the origin and nature of the nebula by looking at its kinematic structure (Taylor 1977; Terrett 1979; Meaburn & White 1982; Huggins & Healy 1986), and a model with a thick, radially expanding, toroidal ring is preferred over models involving a radially expanding helix.

Walsh & Meaburn (1993) counted some 600 cometary knots in their Hα + [N II] 6584-Å images, although higher resolution *HST* imagery has led O'Dell & Handron (1996) to estimate 3500 for the entire nebula. The images of Walsh & Meaburn (1993) also indicate that there are no knots close to the central star, but that they occur in some numbers around the periphery of the inner, low-ionization, helical structure. A comparison of Hα + [N II] 6584-Å and [O III] 5007-Å images of the knots (Meaburn et al. 1992; Walsh & Meaburn 1993) allows one to determine if the knot is on the near or far side of the central high-ionization region. Knots which are bright in Hα + [N II] 6584 Å but which appear *in absorption* in [O III] 5007 Å are on the near side. The dense, dusty core of the knot is absorbing and scattering the background [O III] 5007-Å radiation, and hence appears dark. Similarly, knots which are bright in Hα + [N II] 5486 Å and do not show as dark patches in the [O III] 5007-Å image must either be on the far side of the [O III] 5007-Å-emitting regions or far enough to one side so as not to be along the line of sight to the latter.

Not surprisingly, there has been considerable interest in the origin and nature of these knots and their tails. The knots themselves may be formed from Rayleigh–Taylor instabilities at the ionization front while the PN is still young and the central star highly luminous (Capriotti 1973), or formed through instabilities when the hot, fast wind from the central star collides with the slow, higher density red giant wind (Vishniac 1994). Dyson et al. (1989) have suggested that the knots could be remnants of SiO maser spots which were formed in the atmosphere of the AGB star and which have survived ejection and photionization.

The ionization of the surfaces of the tails (which are shadowed by the optically thick knots from direct ionizing radiation from the central star) may be the diffuse radiation field (Kirkpatrick 1972; Van Blerkom & Arny 1972; i.e., Lyman photons from the central star that have been scattered or re-emitted) or via a low-Mach-number flow caused by the interaction with a low-velocity wind, perhaps arising in the expanding ionized gas rather than in the stellar wind itself (Dyson, Hartquist & Biro 1993; Hartquist & Dyson 1993).

In Meaburn et al. (1996) we discussed the implications only of the ≈ 10 km s^{-1} global expansion of the system of cometary knots and found that this was 14 km s^{-1} less than the overrunning material which was considered to be the central [O III] 5007-Å-emitting shell. This view is significantly refined in the present paper. Here also we present the volumetric imagery (i.e., position/velocity data cubes) of a significant subset of the knots, from which we were able to determine their global motions described in Meaburn et al. (1996). The results from this process are presented in detail and now interpreted in more advanced ways, since a clear relationship between the global expansion of the knots and that of the CO-emitting ring has now been established. We also look in detail at the morphology and kinematics of three of the brighter knots and their tails for which spatially resolved Hα, [O III] 5007-Å, [O I] 6300-Å and [N II] 6584-Å profiles and NTT images have been obtained.

2 OBSERVATIONS

The majority of the spectral observations were made using the dedicated Manchester echelle spectrometer (MES) (Meaburn et al. 1984) in combination with the 3.9-m Anglo-Australian Telescope and a Tek 1024 × 1024 CCD detector. Over the eight nights (1994 October 13–20) on which these profiles were obtained, the 'seeing' remained stable at a remarkable 0.8 arcsec, which permitted the partial spatial resolution of the crescent shaped knots which are ≈ 2 arcsec across. All the observations made during this run used a slit length equivalent to 163 arcsec and slit widths of either 70 μm (= 6 km s^{-1} and 0.5 arcsec) or 150 μm (= 10 km s^{-1} and 1 arcsec). All spectral observations were calibrated to ± 1 km s^{-1} accuracy against the spectrum of a Th/Ar emission-line lamp. In each case, individual echelle orders containing the emission line(s) of interest were isolated using interference filters.

Observations using a long multislit were made of three rectangular areas covering most of the knots. For these, MES was used in its primary spectral mode with a 10-Å-bandwidth filter isolating the 87th echelle order containing the [N II] 6584-Å emission line. Three data 'cubes' (each with two spatial and one velocity dimension) of line profiles over three separate areas of the Helix nebula were obtained from the regions indicated in Fig. 1. These regions cover some 195 of the most prominent Helix knots. For each cube a 10-element multislit, orientated east–west (EW), was stepped 10 times by 1 arcsec in a north–south (NS) direction. The separation of individual slits was 11.2 arcsec corresponding to 138 km s^{-1}, and the slit widths were 70 μm. In all, 30 separate integrations, each of 1800-s duration, were obtained. An example of one of the integrations is shown in Fig. 2. In effect, spatially resolved [N II] 6584-Å profiles were obtained along 300 EW slit lengths. The brightest cometary knots are identified as 1–50 in Figs 3(a)–(d).

A prominent knot (14 in Fig. 3b) was observed in detail using MES in its single long-slit slit mode (150-μm wide) through filters which isolated the echelle orders 87 (for Hα and [N II] 6584 Å) and 114 for [O III] 5007 Å. The EW long-slit position was moved with 1 arcsec NS steps between five integrations, each of 1800-s duration, for the Hα and [N II] 6584-Å observations of Knot 14. [O I] 6300-Å profiles along one EW slit position were detected from Knot 14 in the 91st order with a 70-μm-wide slit. The bright airglow [O I] 6300-Å line was used to calibrate this observation to ± 0.5 km s^{-1} in absolute radial velocity. The integration time was 1800 s. The heads of two other prominent knots (38 and 1) were observed only in the [O III] 5007-Å line in the single-slit mode.

Finally, again with MES in its single long-slit mode, Hα and [N II] 6584-Å line profiles of the host nebula were

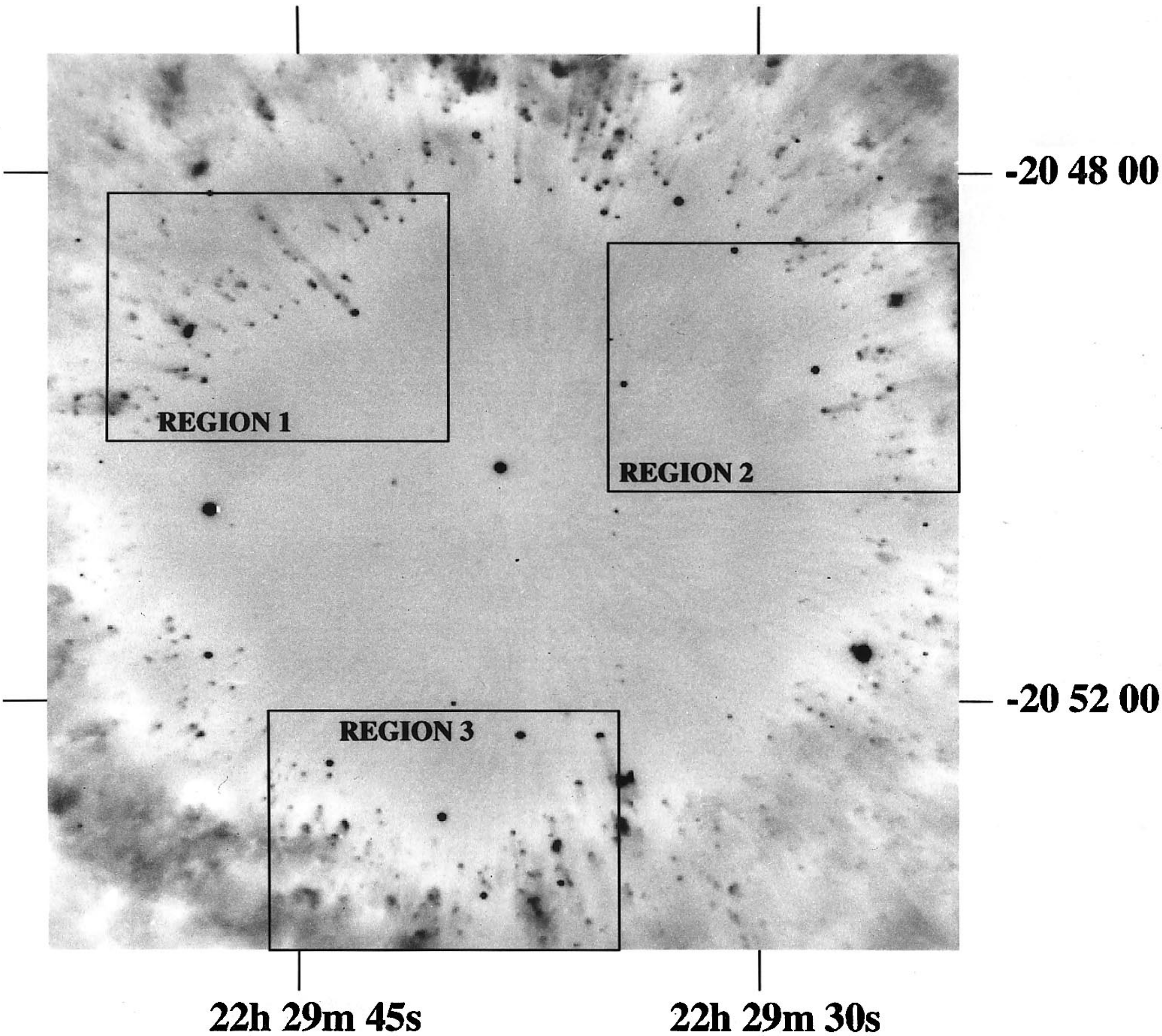

Figure 1. An image of the central region of the Helix nebula in the light of Hα + [N II] 6584 Å, showing the numerous ionized knots. The three regions marked are the areas from which the cubes of stepped, multislit data, in the light of [N II] 6584 Å, were obtained. North is to the top.

© 1998 RAS, MNRAS **294**, 201–223

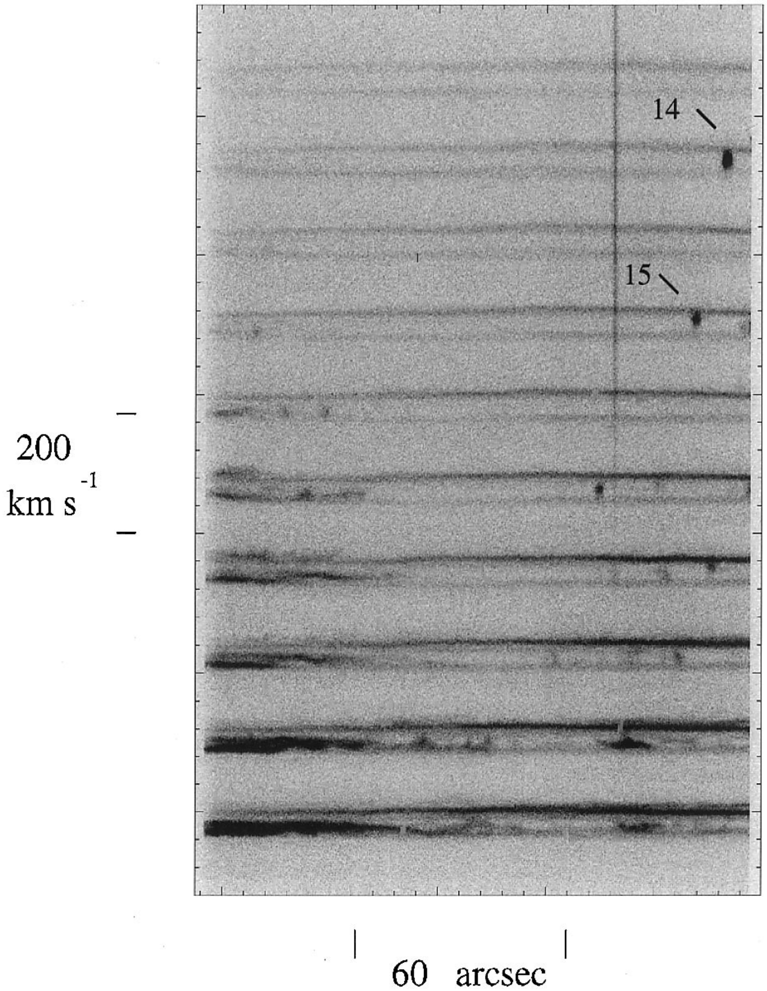

Figure 2. An example of one of the 30 10-element multislits [N II] 6584-Å spectra from which the data cubes were constructed. East is to the right. The many detached knots of emission (between the [N II] 6584-Å tramline emission from the Helix nebula itself) are from the ionized knots. Emission from two of the knots identified in Fig. 3 is indicated. The vertical line is stellar continuum from a field star lying on one of the multislit elements.

observed along lines of EW and NS observations that passed through the central star to cross the outer low-ionization helical structure. Most of these slit positions were obtained during the same observing run as the multislit data, using a slit width of 150 μm. The positions of the eastern leg of the EW cut were obtained with the AAT and MES in 1984, using a 70-μm slit width and the IPCS detector (Walsh & Meaburn 1987). One EW long-slit position (70-μm slit) was obtained over the central star to obtain [O III] 5007-Å profiles. These observations provided the global kinematical framework within which the motions of the cometary knots can be interpreted.

An EW slit length over the head and tail of Knot 1 and other nearby knots was obtained in good seeing (≤ 1 arcsec) with a 1.0-arcsec-wide single slit in 1994 June with the EMMI spectrometer on the NTT. The detector was a 2048×2048 Tek CCD with 24-μm pixels ($\equiv 0.27$ arcsec).

For these observations the 31.6 groove mm^{-1} echelle (#10) was used, and order 87 was isolated by the same Hα + [N II] 6584-Å filter used for imaging. Spectra of the Hα and [N II] 6584-Å emission lines along a slit length of 7.6 arcmin were thus obtained. The exposure time was 1800 s. The data were reduced identically to the MES long-slit data.

Wide-field imaging observations of the core of NGC 7293 were obtained with the ESO New Technology Telescope (NTT) in 1992 August. The RILD mode of EMMI was used with a Thomson THX 1024×1024 CCD with 19-μm pixels, covering the central 7.5×7.5 arcmin^2 of the Helix nebula (0.44-arcsec pixels). Images with an Hα + [N II] 6584-Å filter (centre 6570 Å, width 72 Å) and an [O III] 5007-Å filter (centre 5014 Å, width 56 Å) were obtained in seeing of ≈ 1 arcsec. A series of six Hα + [N II] 6584-Å images, each of 300-s duration, and three [O III] 5007-Å images, each with 600-s exposure time, were made. Bias and flat-fields were also taken, but no photometric standards. The data were reduced by subtracting bias and normalizing by the flat-field.

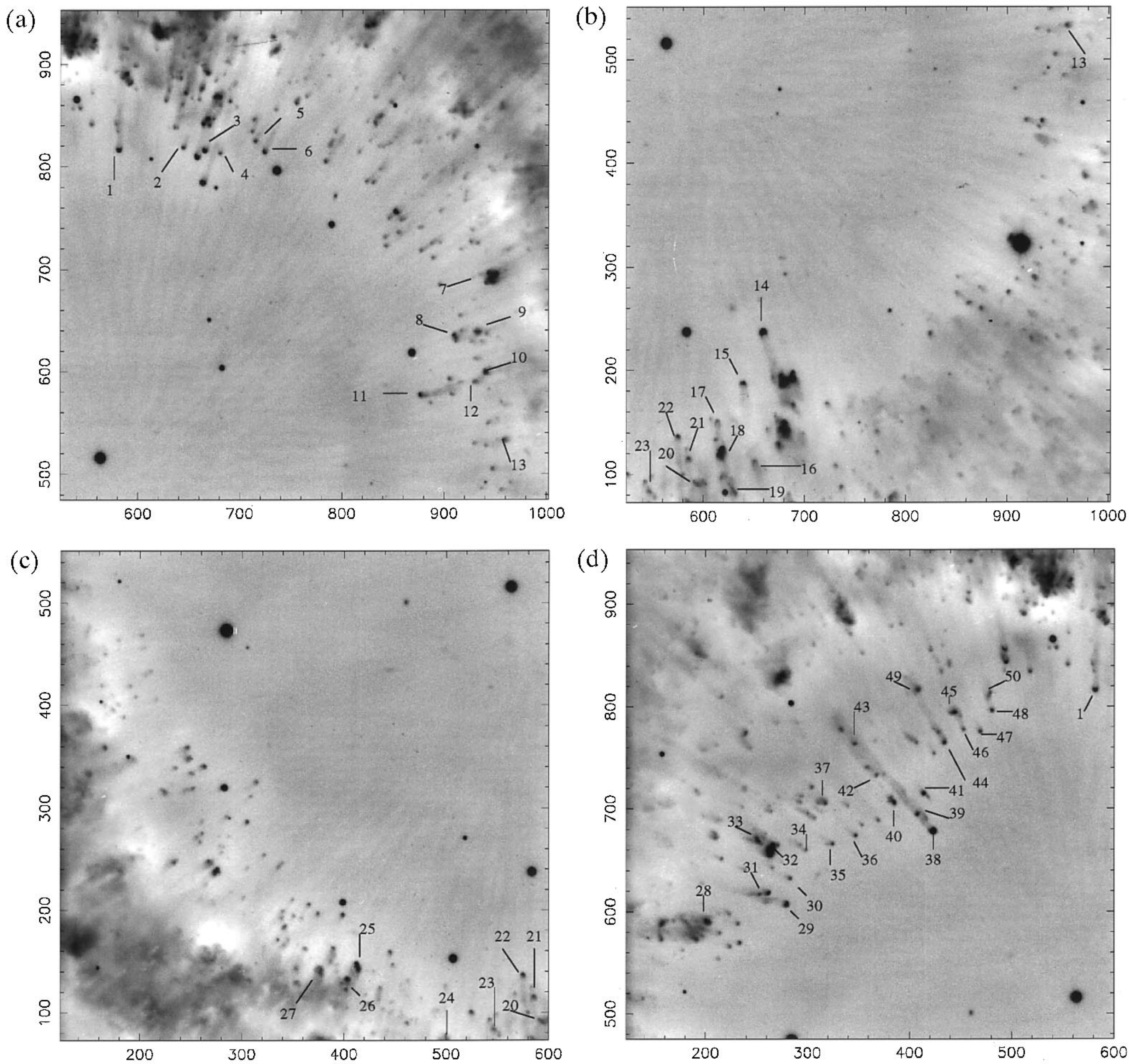

Figure 3. The 50 knots listed in Table 2 are identified on unsharp masked Hα + [N II] 6584-Å images of the core of the Helix nebula. Knot 1 in (a) is identified as C1, Knot 14 in (b) as A2, and Knot 38 in (d) as B1 by Huggins et al. (1992).

3 MULTISLIT ANALYSIS AND RESULTS

The multislit data were manipulated (Clayton 1987) to produce three-dimensional data blocks (or cubes) with one axis (X) in the EW direction along the slit, another axis (Y) in the NS direction in which the telescope was stepped and the last axis (Z) in the direction of dispersion. These data cubes are effectively a stack of images of the source, each containing the emission for the gas moving within a small radial velocity range. An array showing a series of slices from one of the data cubes is illustrated in Fig. 4. Each image includes [N II] 6584-Å emission from a range of radial velocities, as indicated in Table 1. All radial velocities quoted in this paper are heliocentric unless otherwise stated. The images have been rebinned to give the correct aspect ratio.

The radial velocities of 50 of the ionized knots, mostly from Regions 1–3, were determined from the spectra. In each case, a single [N II] 6584-Å profile from the brightest region just behind the apex of each clearly identified knot was simulated by a single Gaussian, and its heliocentric radial velocity $V_{\rm HEL}$ measured. The radial velocities of the 50 most prominent knots could be measured in this way to ± 2 km s^{-1} accuracy from the present data set. A parallel inspection of the [O III] 5007-Å image of the whole central region of the helix nebula was used to determine whether or not a knot has a heavily absorbing core, and is therefore on

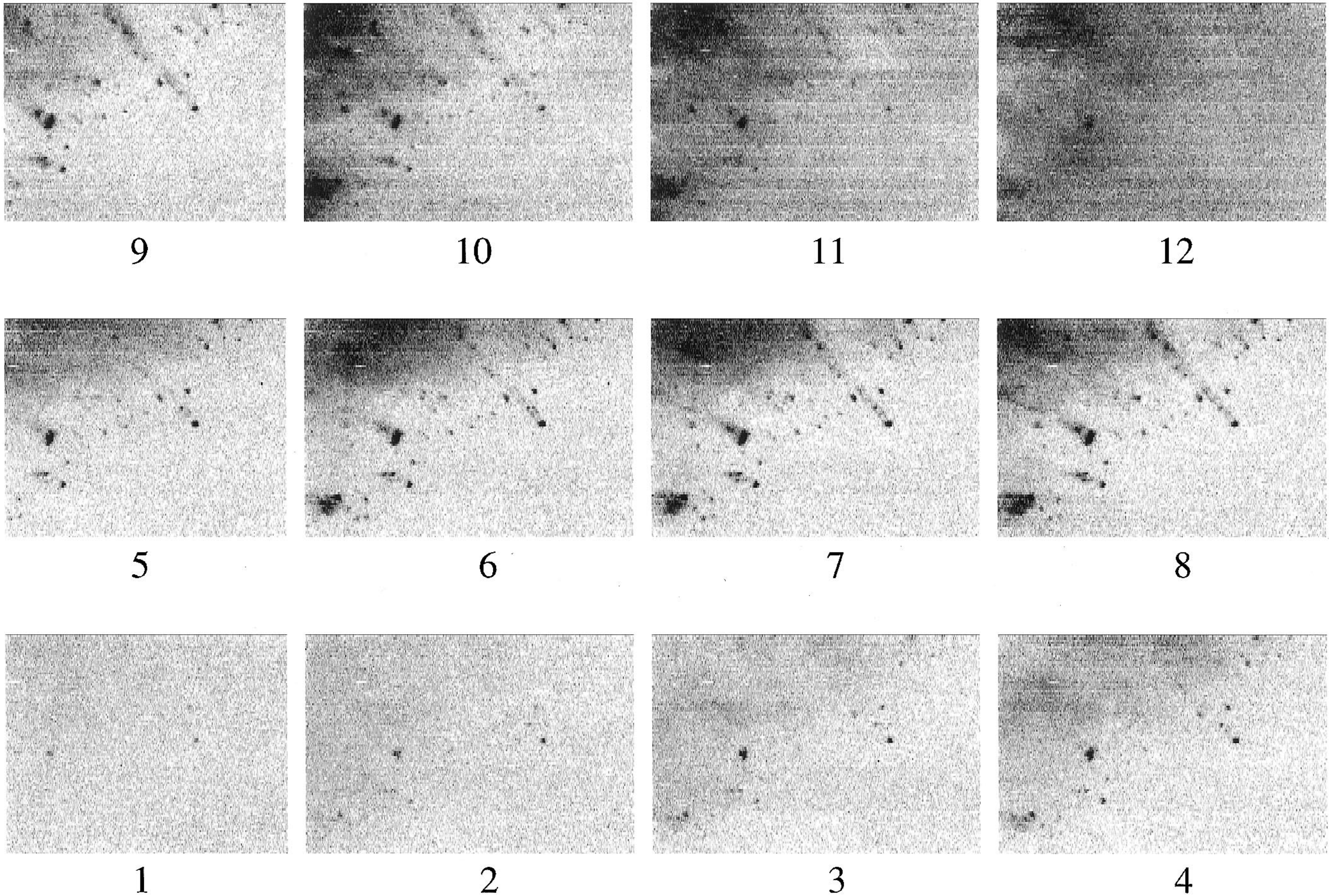

Figure 4. An array of [N II] 6584-Å 'velocity images' from Region 1. The velocity range covered by each of the images is given in Table 1.

© 1998 RAS, MNRAS **294**, 201–223

Table 1. Radial velocity ranges of the image in Fig. 4 (Region 1).

Frame Number	Heliocentric Velocity Range (km s^{-1}) Region 1		
1	−37	⟶	−36
2	−34	⟶	−33
3	−31	⟶	−30
4	−29	⟶	−27
5	−26	⟶	−24
6	−23	⟶	−21
7	−20	⟶	−19
8	−17	⟶	−16
9	−14	⟶	−13
10	−12	⟶	−10
11	−9	⟶	−7
12	−6	⟶	−4

the near side of the central, [O III] 5007-Å-emitting region, or only mild absorption, and so on the far side (see Meaburn et al. 1992). The heliocentric radial velocities (V_{HEL}) of 50 of these knots are listed in Table 2, and the identity of each of these knots is indicated in Figs 3(a)–(d). The images in Figs 3(a)–(d) clearly show the tails associated with each knot, which point away from the central star. They also show the crescent-shaped heads of some of the brighter knots. (N.B., $V_{\mathrm{HEL}} = V_{\mathrm{LSR}} - 3.2$ km s^{-1} throughout the present paper.)

4 GLOBAL MOTIONS

4.1 Motions of the host nebula

The cometary knots form a distinct population within the [N II] 6584-Å bright nebular shell of NGC 7293, and to understand their nature it is important to compare their kinematics with the global motions of the host nebula. To this end, two 'superlong slit' observations along the EW and NS diameters were made. The NS cut contains a series of (lengthways) overlapping single-slit observations, which were wavelength-calibrated in the usual way and then combined using the Starlink CCDPACK package to produce a single position–velocity (pv) data array equivalent to one, ~740-arcsec-long, single slit. The mosaicking program automatically applied both zero-point and scale corrections to each individual frame, based on the overlapping regions,

Table 2. Heliocentric radial velocities for Helix knots identified in Fig. 3. Knots showing heavy absorption are on the near side of the central [O III] 5007-Å core, whilst those showing mild or no absorption are on the far side.

ID	V_{Hel}	Absorption	ID	V_{Hel}	Absorption	ID	V_{Hel}	Absorption
1	−31.6	Heavy	18	−25.4	Heavy	35	−21.0	Mild/None
2	−30.6	Heavy	19	−21.3	Mild/None	36	−18.9	Mild/None
3	−28.8	Heavy	20	−20.0	Mild/None	37	−15.2	Mild/None
4	−30.2	Heavy	21	−24.0	Heavy	38	−22.5	Mild/None
5	−31.9	Heavy	22	−25.4	Mild/None	39	−23.9	Heavy
6	−29.9	Heavy	23	−21.3	Mild/None	40	−19.0	Mild/None
7	−22.5	Mild/None	24	−21.1	Mild/None	41	−21.5	Mild/None
8	−36.0	Heavy	25	−20.8	Mild/None	42	−15.3	Mild/None
9	−36.9	Mild/None	26	−18.0	Mild/None	43	−16.3	Mild/None
10	−36.4	Heavy	27	−18.3	Mild/None	44	−21.3	Mild/None
11	−32.2	Heavy	28	−23.5	Heavy	45	−19.3	Mild/None
12	−37.0	Heavy	29	−22.9	Heavy	46	−19.7	Mild/None
13	−18.9	Mild/None	30	−21.6	Mild/None	47	−18.8	Mild/None
14	−26.9	Heavy	31	−23.0	Heavy	48	−20.8	Mild/None
15	−32.5	Heavy	32	−20.9	Mild/None	49	−12.6	Mild/None
16	−30.8	Heavy	33	−18.8	Mild/None	50	−19.3	Mild/None
17	−31.8	Heavy	34	−18.7	Mild/None			

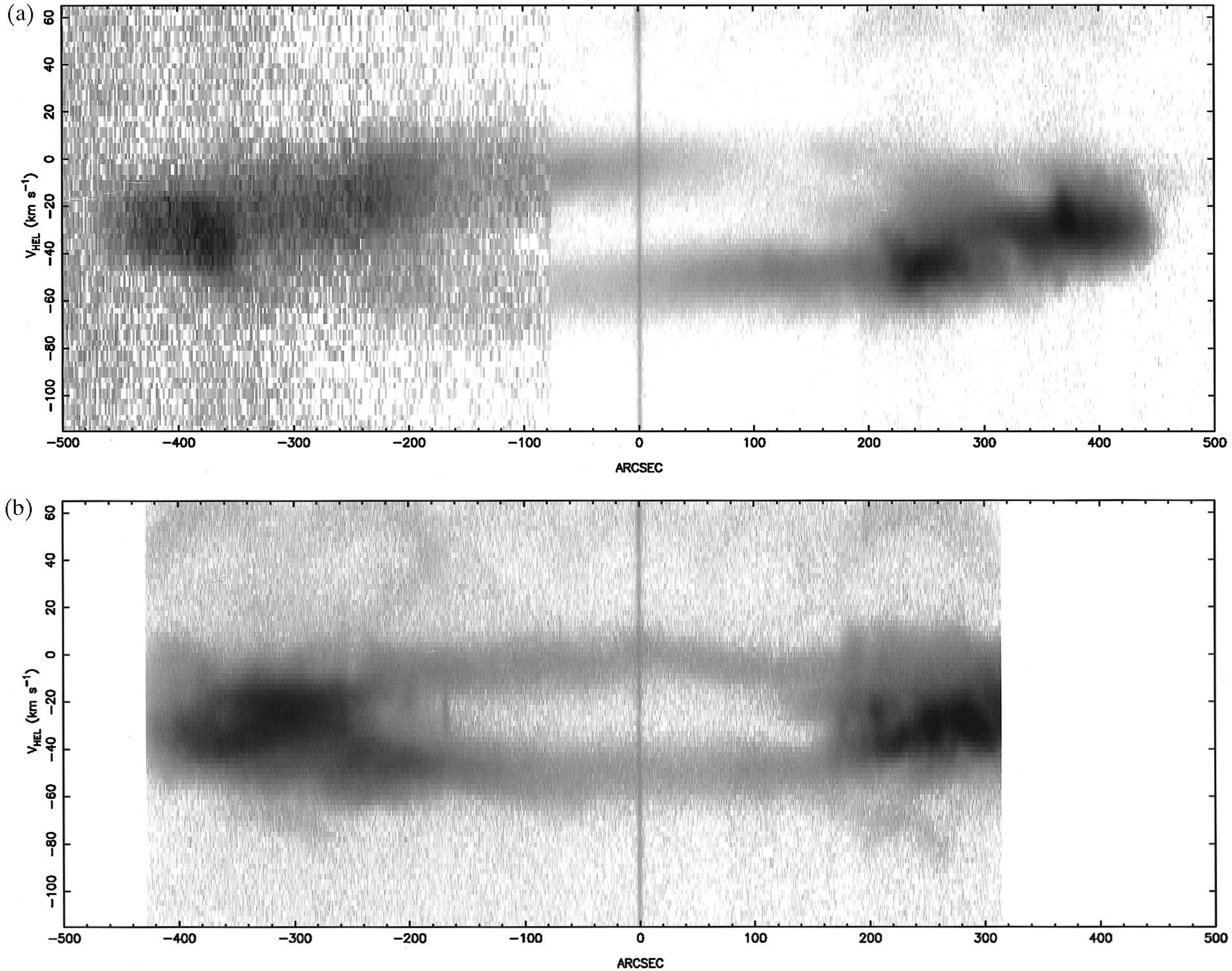

Figure 5. Grey-scale representations of the [N II] 6584-Å pv arrays from (a) the EW and (b) the NS diametric cuts through the main shell of the Helix nebula. The [N II] 6584-Å emission from Knot 22 can be seen within the main velocity ellipse, at a radius of ~ -165 arcsec in the NS cut.

to produce a mutually consistent set of data frames, which were then mosaicked together according to their relative positions along the diametric cut. The same procedure was used to produce the EW cut, except that in this case the data sets comprising the eastern arm of the cut were obtained at an earlier epoch, using the IPCS detector which was set up with a pixel size rather larger than the later CCD pixel size. The eastern and western data sets were mosaicked separately; then the eastern frame was rebinned to the same pixel size as the western frame. A velocity offset was applied to the eastern frame to account for the difference in heliocentric velocity correction between the two epochs, and then the two data frames were mosaicked with zero-point and scale correction to produce the final EW cut.

The EW and NS superlong-slit cuts are shown in Figs 5(a) and (b) respectively as grey-scale pv diagrams. Although the NS cut does show the characteristic velocity ellipse associated with a simple radially expanding shell, the EW cut shows a tilted and incomplete velocity ellipse suggestive of an inclined cylindrical shape with axis of symmetry projected roughly on to the EW axis on the sky, but tilted toward the observer at the eastern end and away from the observer at the western end.

A systemic heliocentric radial velocity for the whole system was derived by considering the separation of the two velocity components at the position of the central star for each cut. This gave a value of $V_{\mathrm{HEL}} = -27 \pm 0.5$ km s^{-1}.

4.2 Motions of the knots from [N II] 6584-Å profiles

The differences in radial velocity of the observed sample of 50 knots compared with the mean systemic radial velocity of the entire nebula ($V_{\mathrm{HEL}} = -27$ km s^{-1}; see Section 4.1) as a function of angular distance from the central star are shown in fig. 3 in Meaburn et al. (1996). As reported in that paper, the group of near-side knots have a distinctly different radial velocity (≈ -12 km s^{-1}) from the far-side group, and a global (although not uniformly spherical) expansion of ≈ 10 km s^{-1} was derived. An even more relevant way of deriving the global expansion of the system of knots has now been devised. This is to show the variation of heliocentric knot radial velocity as a function of position angle (PA) around the face of the nebula (see Fig. 6). The data are plotted over two cycles, with each data point being plotted twice to show the variation with PA more clearly.

The dotted line in Fig. 6 shows the variation of CO velocity around the helical structure of the nebula with PA for radii ≤ 300 arcsec (Healy & Huggins 1990). It is clear in Fig. 6 that the knot radial velocity distribution is generally related to that for CO. Most of the far-side knots (no absorption) are around -20 km s^{-1} clustered on either side of PA 110°, whereas the near-side knots are around -34 km s^{-1} around PA 290°. There are some anomalies to this pattern, i.e., a few far-side knots are also found at PA 290°. These are easily explained in the model described in Section 6.2, where a better value of the global expansion of the system of knots is also derived.

4.3 Motions of the knots from velocity images

An alternative way of appreciating the global motions of the knots is through 'velocity imagery' of the stepped multislit arrays. The images in Fig. 4 show the variation in ionized gas velocity for the most blueshifted material (element 1) to that which is most redshifted (element 12), as detailed in Table 1. These velocity images thus show the trends in velocity for both the background nebular material and, more importantly, for each individual knot. This velocity imaging of the data allows one to study the variation in knot intensity as a function of velocity for all of the knots in a region simultaneously. This cannot be done with the data whilst it is still in long-slit format.

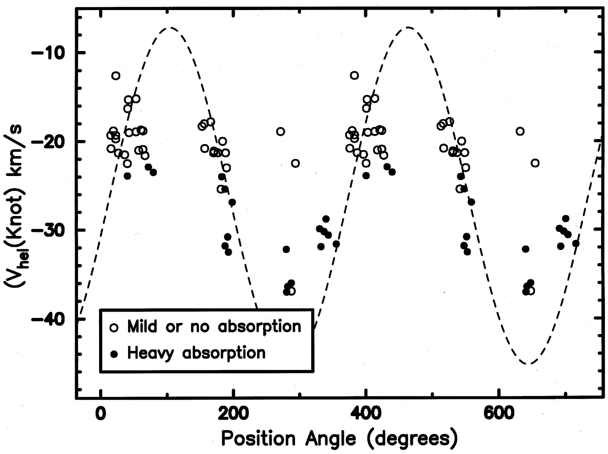

Figure 6. The variation of heliocentric knot velocity as a function of position angle around the face of the nebula. Filled circles indicate which knots are silhouetted against the central, [O III] 5007-Å-emitting shells of the Helix nebula, and therefore on the near side of the nebular centre. Empty circles show those on the far side. The dashed line shows the sinusoid which fits the CO radial velocities (for radii ≤ 300 arcsec) associated with the helical 'rings' of this nebula.

One can see that the knots fall into two groups – those whose intensity peaks are at radial velocities significantly less than systemic (-27 km s^{-1}), and those which peak at a similarly greater velocity. The latter group of knots is more numerous. Walsh & Meaburn (1993) found that some 40 per cent of the knots were found in absorption in [O III] 5007-Å imagery.

5 CASE STUDIES OF INDIVIDUAL KNOTS

5.1 Knot 14

5.1.1 Results

The isolated Knot 14 (see Fig. 3b) is, in projection, one of the closest to the central star and has been detected unambiguously in CO emission by Huggins et al. (1992). The Hα and [N II] 6584-Å-emitting head forms an arc around the [O III] 5007-Å absorbing core, as shown in Fig. 7. It is then identified as a near-side knot in Table 2. The faint arc of [O III] 5007-Å emission around the head of this knot that is contoured in Fig. 7 implies that it is within the O III ionization zone of the Helix nebula, i.e., photons from the central star with energies ≥ 35.1 ev impinge on its surface.

The pv arrays, contoured in Figs 8(a) and (b) respectively, of Hα and [N II] 6584-Å profiles (with the contribution from the host nebula subtracted) from the five EW slit positions

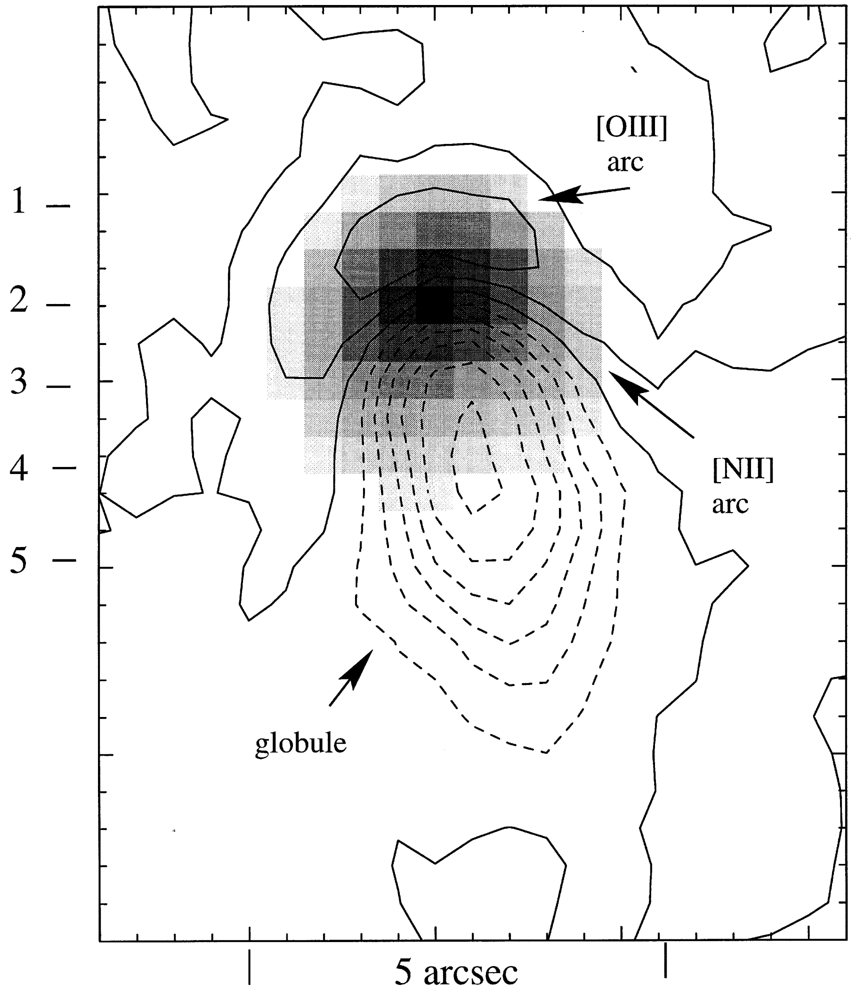

Figure 7. The contours with linear intervals are from the NTT [O III] 5007-Å image of Knot 14. The solid lines (arrowed as '[O III]arc') show the [O III] 5007-Å emission around the head of the globule whose [O III] 5007-Å absorption is depicted by dashed contours (arrowed 'globule'). The [N II] 6584-Å emission (arrowed '[N II] arc') is shown by the negative grey-scale representation from an [N II] 6584-Å image. The slit positions 1–5 are also marked.

marked in Fig. 7, separated from each other by 1 arcsec from north (Slit 1) to south (Slit 5) over the head of Knot 14 reveal significant kinematical changes. For instance, the Hα profiles over the very apex of the knot (Slit 1) have a FWHM of $\approx$50 km s^{-1} and develop a distinct approaching component at $V_{\rm HEL} \approx -50$ km s^{-1} along Slit 3 (2 arcsec south of Slit 1). The corresponding [N II] 6584-Å profiles are narrower and show no wings to negative radial velocities. This behaviour is particularly clear in Figs 8(c) and (d), where sample profiles through the maxima in Figs 8(a) and (b) are shown respectively. However, a systematic shift to more negative radial velocities is apparent in the [N II] 6584-Å profiles in Fig. 8(d) from Slit 1 to Slit 4. This behaviour is depicted in Fig. 9, where the centroids of single Gaussians fitted to the central [N II] 6584-Å profile for each slit position are compared with the CO and [O I] 6300-Å radial velocities. Note that the [N II] 6584-Å profile from Slit 2, which intersects the brightest emission from the knot, when fitted by a single Gaussian, is centred on $V_{\rm HEL} = -28 \pm 1$ km s^{-1}. This should be compared with $V_{\rm HEL} = -25.6$ km s^{-1} given by Huggins et al. (1992) for the CO emission from the central globule, and with -26.1 ± 0.5 km s^{-1} measured here for the [O I] 6300-Å emission (again with a single Gaussian fit). Incidentally, the FWHM of the observed [O I] 6300-Å profile from Slit 2 over Knot 14, when corrected for instrumental broadening (taken to be the width of the profile of the airglow [O I] 6300-Å emission) is 9.1 km s^{-1}. This should be compared with the much broader [N II] 6584-Å and Hα profiles from this position shown in Figs 8(a)–(c) (even when these are corrected for the 10 km s^{-1} width of the instrumental profile). The observed kinematics described in this section are modelled and explained in Section 5.1.4.

The background-subtracted Hα profiles for Slits 4 and 5 in Figs 8(a) also reveal absorption of the emission at more positive radial velocities. This behaviour is revealed more clearly in the [O III] 5007-Å profiles over the head of Knot 14. The dusty core of the knot can be seen in the contoured and grey-scale representation of the long-slit array of [O III] 5007-Å profiles in Fig. 10(a) to absorb only the receding

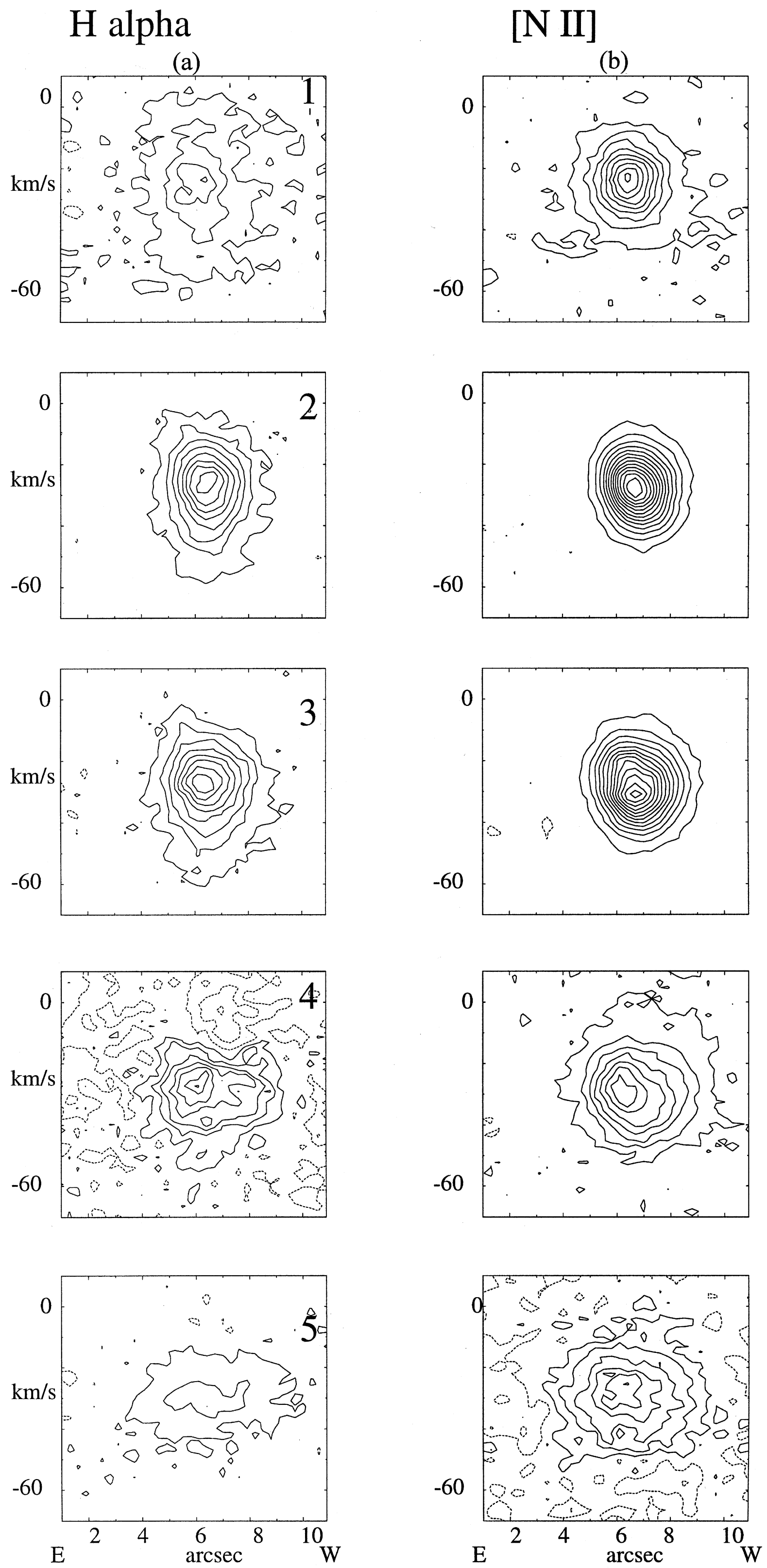

Figure 8. Contour maps of (a) the Hα and (b) [N II] 6584-Å pv arrays for EW Slits 1–5 over the head of Knot 14. Equally spaced linear contours are shown. The slit positions are separated by 1 arcsec, with Slit 1 being the most northerly over the very apex of Knot 14 (see Fig. 7). Heliocentric radial velocities are shown. (c) Sample Hα line profiles through the brightness peaks of the pv arrays in (a). (d) Sample [N II] 6584-Å line profiles through the peaks in (b). (e) The pv arrays of [N II] 6584-Å line profile predicted by the morphological and kinematical model. These should be compared with the observations in Fig. 8(b).

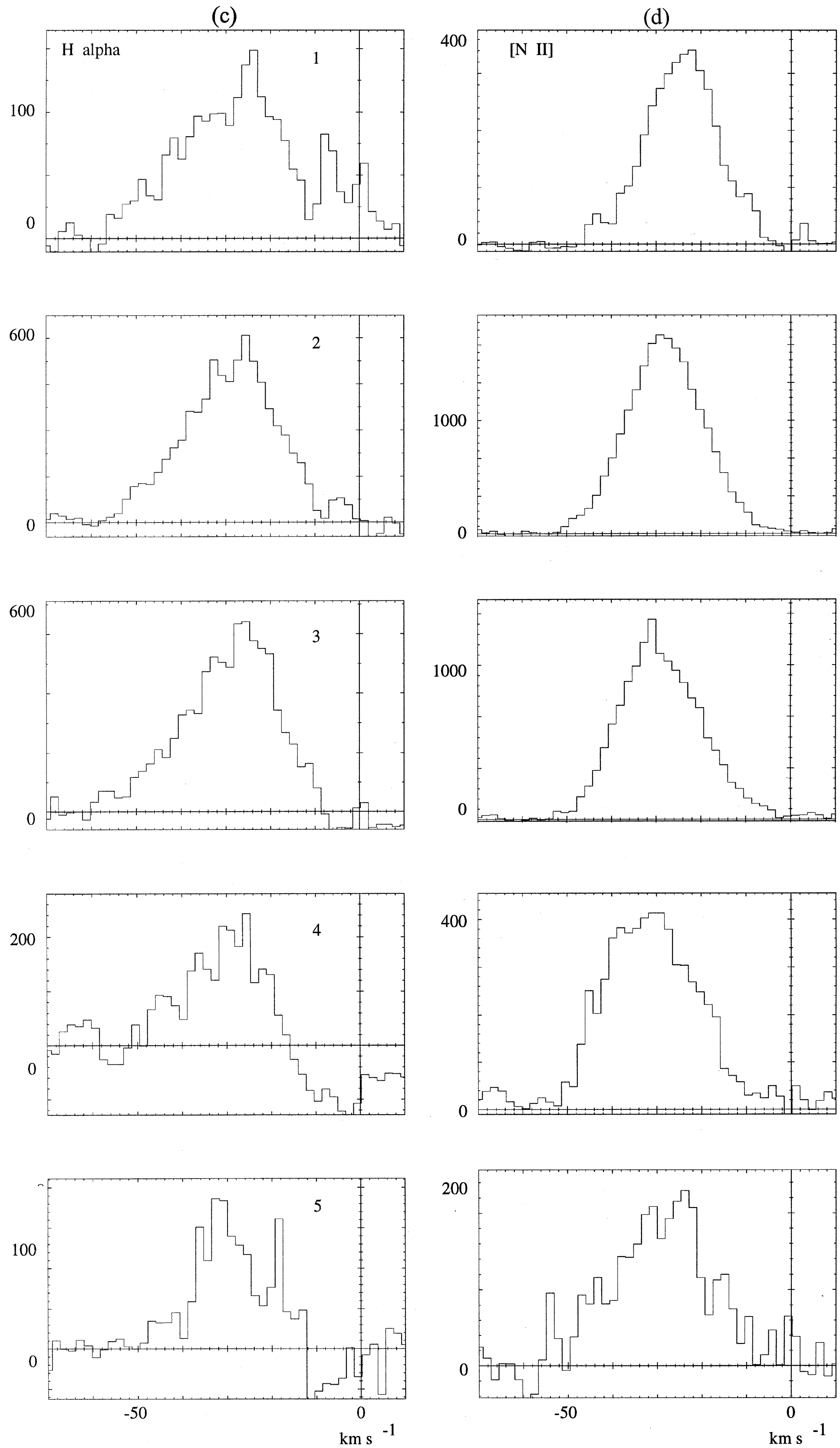

Figure 8 – *continued*

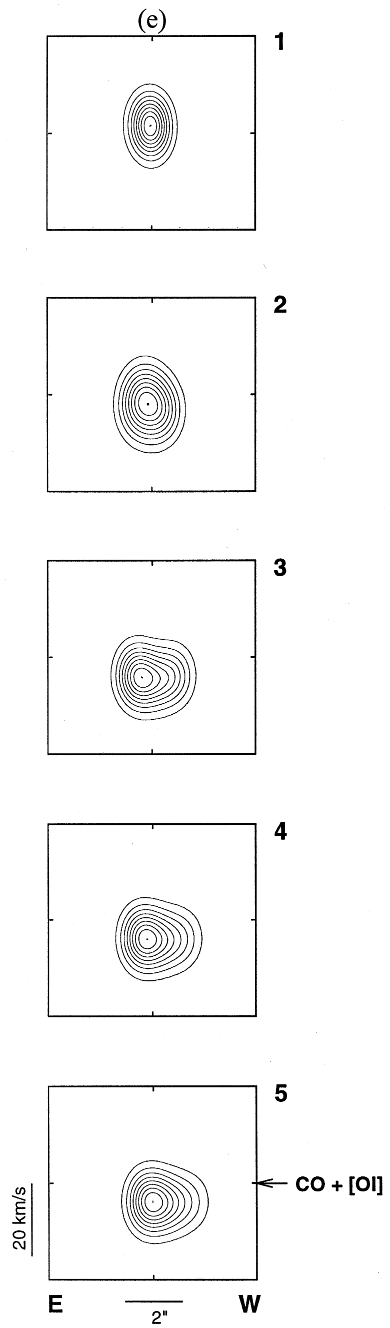

Figure 8 – *continued*

components of the [O III] 5007-Å emission from the host nebula (and see Fig. 11a). The depth of this absorption is illustrated in Fig. 11(b), where the relative surface brightness is plotted along the same length of the slit, but now only in the range of receding radial velocities ($V_{\rm HEL} = -29.5$ to 5.6 km s^{-1}) where absorption is observed in Fig. 10(a). At the minimum of transmission in Fig. 11(b) the fraction of background [O III] 5007 Å transmitted is 0.53. The halfwidth of this absorption feature is measured as 2.2 arcsec which, when corrected for the $\approx$1-arcsec seeing that prevailed, gives a globule width of 2 arcsec, and 0.48 as the fraction of background [O III] 5007 Å transmitted at the minimum of transmission. The depth of the [O III] 5007-Å absorption component for receding radial velocities is far more pronounced in Figs 10(a) and 11 than for the corresponding feature in the Hα profiles (Slits 4 and 5 in Figs 8(a) and (c)). This implies, as expected, that there is far less [O III] 5007-Å-emitting gas from the host nebula along the near-side sight line to the globule, to fill in the absorption, than Hα emission at the minimum of transmission.

The faint arc of [O III] 5007-Å emission around the head of Knot 14 (shown in Fig. 7) implies that it should manifest itself as a feature in the [O III] 5007-Å line profiles of the knot. A candidate for this interpretation is the localized maximum with $V_{\rm HEL} \approx -45$ km s^{-1}, adjacent to the negative velocity absorption feature of the knot, in the section of the [O III] 5007-Å pv array now contoured in Fig. 10(a). The [O III] 5007-Å emission from the surface of the knot itself appears clearly as a component in the profile at approaching radial velocities ($V_{\rm HEL} = -48$ km s^{-1}) with respect to the centroid of the [N II] 6584-Å profile from the same region (at $V_{\rm HEL} = -28$ km s^{-1} along Slit 2 in Figs 8b and d).

5.1.2 *Globule mass and density*

The detection of the dusty, molecular globule as an absorption feature in only the receding components of the [O III] 5007-Å long-slit spectrum of Knot 14 now permits a more accurate estimation of its mass and molecular density than that derived only by imagery in Meaburn et al. (1992).

For Knot 14 the seeing-corrected, minimum fraction of [O III] 5007-Å transmitted (see Section 5.1.1) is 0.48, which implies a logarithmic extinction coefficient of $c = 0.330$ to give $E(B-V) = 0.225$. For a distance of 130 pc and a projected globule diameter of 2 arcsec, a globule mass of $m_{\rm g} = 2.1 \times 10^{-5}$ M$_\odot$ and the mean H$_2$ number density of $n_{\rm g} = 8.9 \times 10^5$ cm^{-3} are implied after application of the relationships of Bohlin, Savage & Drake (1978) and Hildebrandt (1983) in exactly the same way as in Meaburn et al. (1992) (The gas/dust mass ratio of 100/1 of the general interstellar medium is assumed from values quoted in Meaburn et al. 1992).

These parameters should be compared to those of $m_{\rm g} = 1.5 \times 10^{-5}$ M$_\odot$ and $n_{\rm g} = 3.8 \times 10^5$ cm^{-3} for the molecular globule associated with Knot 14 as estimated by Huggins et al. (1992) from CO observations. The CO beamwidth encompassed the whole globule

5.1.3 *Knot kinematics*

Knot 14, similar to all other Helix knots, is a radiatively ionized arc on the surface facing the central star of a dense molecular globule (Meaburn et al. 1992; O'Dell & Handron 1996). Various aspects of the kinematics of Knot 14 can then be explained within the present observations. The [O I] 6300-Å emission will originate from the front surface of the molecular globule, behind the hydrogen ionization front. It should exhibit (as found here) nearly the same radial velocity as the CO-emitting region. However, the greater FWHM of the corrected [O I] 6300-Å profile ($\approx$9.1 km s^{-1}; see Section 5.1.1) compared with 1.9 km s^{-1} for the CO profile is indicative of higher turbulence and temperature in the [O I] 6300-Å-emitting zone.

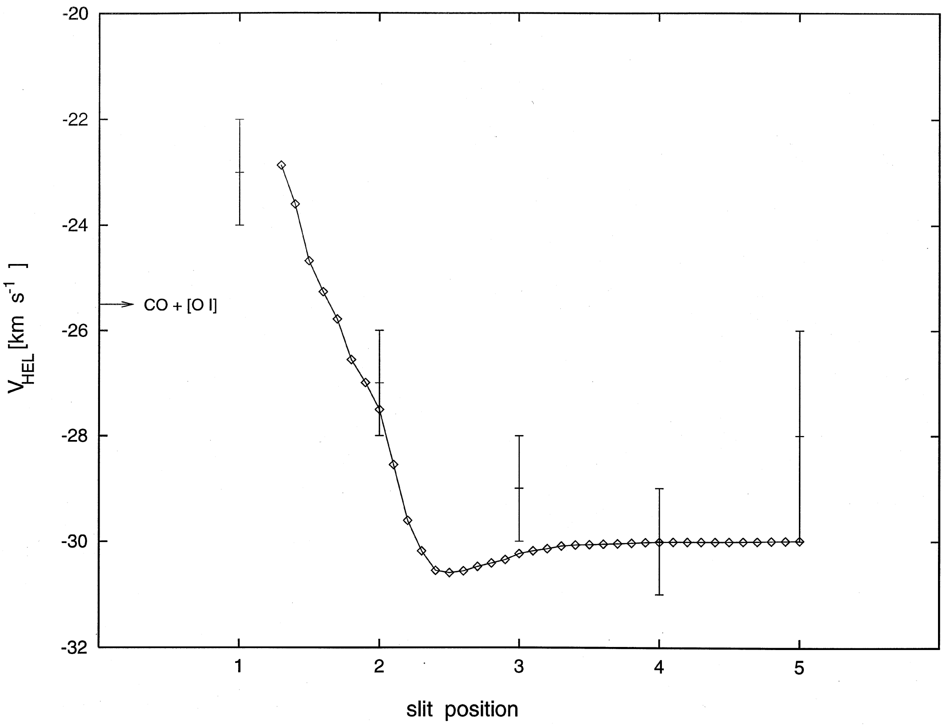

Figure 9. Observed line centres are plotted with error bars for the five slit positions (1–5). These are separated from each other by 1 arcsec. The solid line joins points from the model simulation. The CO and [O I] 6300-Å heliocentric radial velocities for Knot 14 are indicated.

The next relatively narrow layer, just outside the ionization front, will emit [N II] 6584 Å. Here the shift to more negative radial velocities for the profile from Slit 2 compared to that for Slit 1 (Fig. 8d; see Fig. 9 for all slit positions) could be a manifestation of gas flowing around the apex of the molecular globule. A starting point to understanding the kinematics of Knot 14 has therefore been made by modelling the [N II] 6584-Å region as though the [N II] 6584-Å-emitting gas is flowing parallel to the surface of the interior globule. The increased broadness of the Hα profiles, which originate in both the [N II] 6584-Å-emitting region and the lower density gas beyond this, is ignored in this initial process.

5.1.4 Modelling the [N II] 6584-Å flow

Given the observational constraints on the geometry and kinematics of Knot 14, it is possible to model the [N II] 6584-Å-emitting region of this knot and determine its velocity field and true orientation in space. This has been carried out using the SHAPE modelling code (Steffen, Holloway & Pedlar 1996), which calculates long-slit pv arrays for an arbitrary orientation of a given emissivity and velocity distribution in space. Observational parameters such as the slit width, slit position, seeing and velocity resolution are also included in determining the model output.

In our model for the [N II] 6584-Å emission around Knot 14 we assume an emission and velocity distribution similar to a stationary radiative bowshock, i.e., the flow is entirely along the emitting surface. The thickness of the emitting region around the knot is taken to be $\approx$20 per cent of the radius of the knot, similar to the value indicated by *HST* observations (O'Dell & Handron 1996). The emission region is assumed to be optically thin, except for the globule, which absorbs all emission originating from behind it with respect to the observer's line of sight. The shape of the emitting region is taken to be axisymmetric and given by the radius $r(z)$ as a function of distance z from the apex:

$$r(z) = (\xi + 1)\, z^{1/(\xi+1)}, \tag{1}$$

where ξ is a constant determining the curvature of the flow near the apex. This reproduces well the shape of the bright emission around the globule, although the cylindrical tail can obviously not be included in this description with a constant value for ξ. We found that a constant ξ is sufficiently accurate for the region of interest, and it considerably simplifies computational treatment. The velocity of the gas in the rest-frame of the environment is then:

$$\mathbf{v} = \{v_r, v_z\} = \frac{v_b}{1+g^2}\{g, 1\} + \{0, -v_b\}, \tag{2}$$

where v_b is the knot/wind speed differential, and $g = z^{\xi}$. We use a simple analytical description of the emissivity distribution as a function $\epsilon(z)$ of distance z from the apex:

$$\epsilon = \epsilon_0 \exp\left(-\frac{z^2}{2\kappa w^2}\right), \tag{3}$$

where w is the distance at which the emissitivity decreases to $\epsilon_0/2$, and $\kappa = 0.849$ is a scaling constant.

Our best-fitting model of the observations in terms of

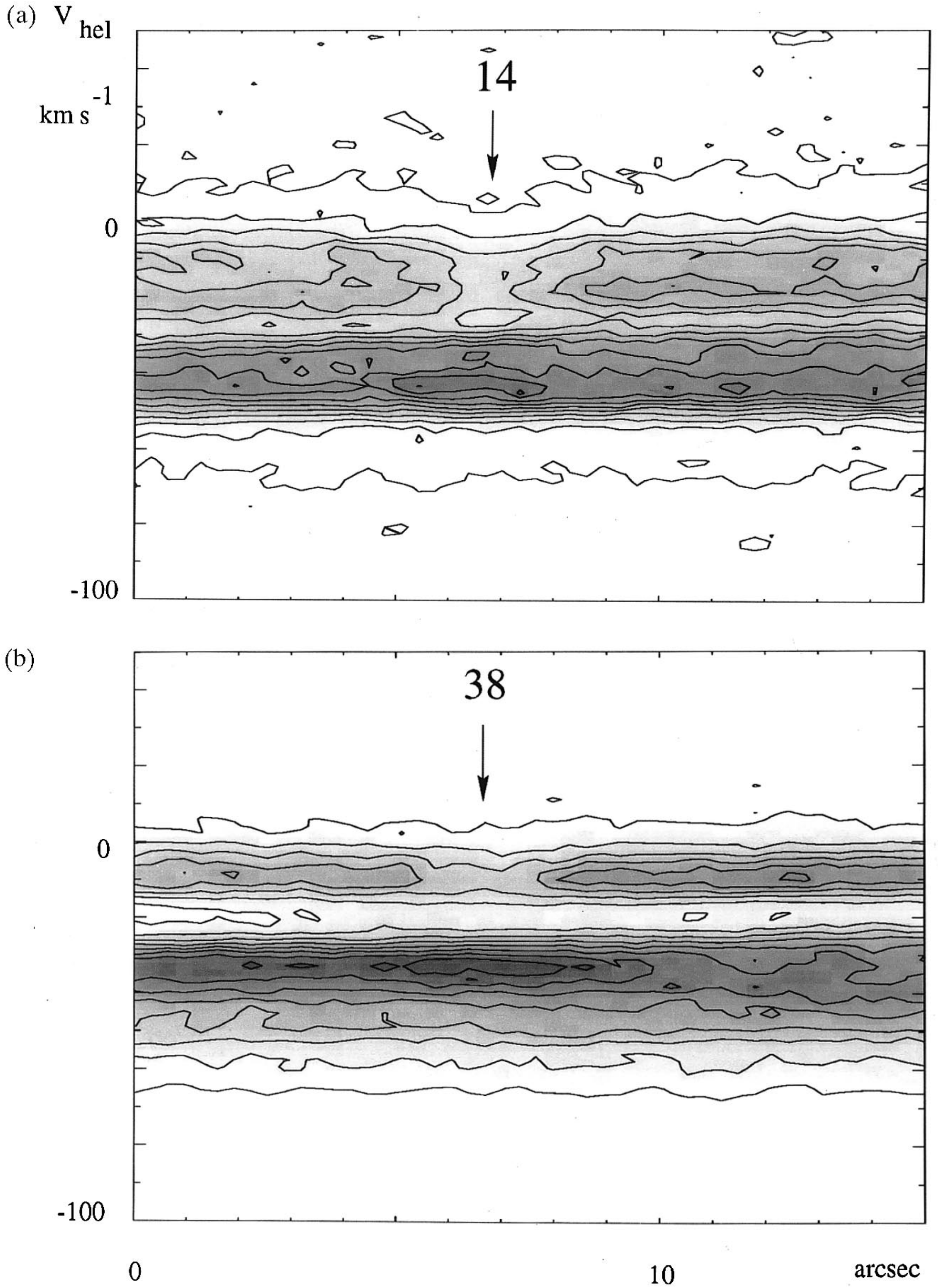

Figure 10. Contour maps, with linear intervals of the [O III] 5007-Å pv arrays for EW slits over (a) Knot 14 and (b) Knot 38. The absorption in the receding [O III] 5007-Å velocity components of the host nebula and the local maxima associated with the two knots, coincident with the approaching velocity components, are apparent.

both the pv arrays and the velocity shift down the knot was found using the parameters listed in Table 3. The resulting pv arrays generated for the simulated slit positions are shown in Fig. 8(e).

The model pv arrays of [N II] 6584-Å profiles (Fig. 8e) show the same gross features as those from the observations (Figs 8b and d); i.e., the increase in extension in the spatial direction, and the trend of the position of maximum inten-

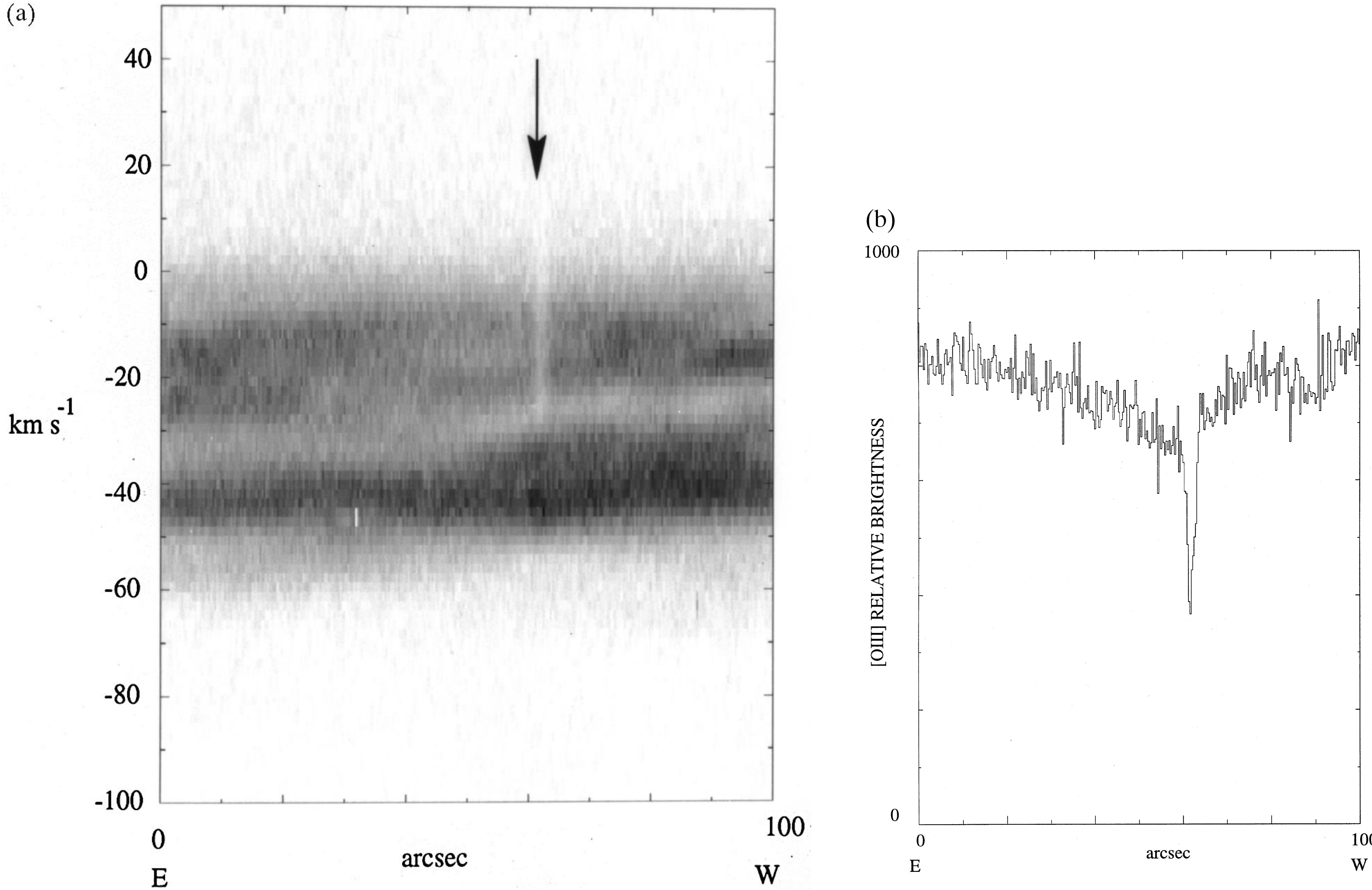

Figure 11. (a) A grey-scale representation of the [O III] 5007-Å profiles contoured in Fig. 10(a) where the length along the slit corresponds to that in Fig. 11(b). The absorption by Knot 14 is arrowed. (b) The brightness variations along the same pv array as in Figs 10(a) and 11(a) but only of the receding velocity components in the [O III] 5007-Å line profiles (with the spectrum of the background light subtracted). The depth of the absorption feature associated with Knot 14 is apparent.

Table 3. Model parameters for Knot 14.

Shape parameter ξ	3.5
Globule radius	1.5″
Globule position from apex	1.75″
Emissivity half length w	3.5″
Velocity v	10 km s^{-1}
Angle to slit	15°
Angle to plane of the sky	25°
Seeing	1″
Velocity resolution	12 km s^{-1}
Slit width	1″

sity to move along the slit. These can be attributed to the increasing radius of the emission region and the slit inclination to the axis of the flow. The velocities of the peaks in the spectral distributions have been plotted in Fig. 9 for each of the simulated slit spectra, along with the observed velocity shifts. A shift in radial velocity of 6 km s^{-1} occurs as the slit is positioned further down the tail. This shift occurs near the head of the flow, similarly to what is found in the observations. Due to the absorption of emission with positive radial velocities by the globule, there is a small minimum after the fast decline in peak velocities. Unfortunately, at the sampling of the observations this minimum is missed, and it would not have been detected in the simulation either had they been sampled at the same positions.

Using the value obtained from the CO measurements of $V_{sys}=-25.6$ km s^{-1} for Knot 14, the shift found in the simulation reproduces the observed value within the errors of measurement. This model requires a flow velocity of 10 ± 3 km s^{-1} in the tail, which is ≈ 17 km s^{-1} less than the differential between the global expansion velocity of the knots and the overflowing wind within the model described in Section 6.2. This could indicate that ionized gas evaporating from the surface of the globule mass loads the lower density wind and, by momentum conservation, reduces the speed of the flowing gas considered here. The inclination angle of $25°\pm5°$ to the plane of the sky with the tail pointing towards the observer is unambiguous, given that the knot is located near to the line of nodes of the main Helix ring.

The approaching velocity components in the broader Hα profiles, particularly those from the apex of Knot 14 (Slit 1 in Figs 8a and c), could be some manifestation of the gas, beyond the [N II] 6584-Å-emitting 'skin', which is overflowing the knot at the mildly supersonic speed of 17 km s^{-1}. This outer ionized zone is within the harder radiation field of the central star for Knot 14 and has an [O III] 5007-Å-emitting head (see Fig. 7).

5.2 Knot 38

Knot 38 is of especial interest for its projected distance to the central star is smallest and it has the most spectacular tail (see Figs 3d, 4 and 12), which points directly away from the central star. Moreover, Huggins et al. (1992) have detected CO emission from the associated molecular globule. The variation in tail morphology as a function of velocity, seen in Fig. 12, indicates that the tail brightness peaks at more positive radial velocities as one moves down the tail away from the knot itself.

Knot 38 shows low absorption in [O III] 5007 Å, indicating that it is on the far side of the central [O III] 5007-Å-emitting region. If one assumes that the tail is pointing directly away from the central star, then the tail must also be pointing away from the observer at some angle. Hence the velocity trend away from the knot and along the length of the tail would indicate an acceleration of the tail material, with the mean radial velocity of material at the end of the tail (in the reference frame of Knot 38 and along the line of sight) being some 9 km s^{-1} more positive than that at the head (see Figs 12 and the [N II] 6584-Å line profiles from different positions in the tail in Fig. 13). It is not possible to deproject the tail in order to obtain absolute velocities since, although we know that Knot 38 is on the far side of the nebula, its *exact* location along the line of sight is not known.

The linear form of the tail of this knot over a large distance suggests that the change in radial velocity is not due to a change in the angle of the tail to the line of sight. This leaves the explanation that the change in velocity is due to an acceleration of the emitting material.

If the maximum possible velocity that this material can obtain is the wind/knot differential velocity of 17 km s^{-1} (see Section 6.2), then the observed increase of 9 km s^{-1} provides a lower limit on the inclination angle of 32°.

5.3 Knot 1

From the [O III] 5007-Å images in Meaburn et al. (1992) the absorbing core and tail of Knot 1 (see Fig. 3a) were shown to be just resolved by the $\approx$1-arcsec resolution imposed by atmospheric 'seeing'. The fractional transmission measured for the core of the knot in that paper also assumed that all of the [O III] 5007-Å emission from the host nebula was on the knot's far side. This left two questions unanswered. Did the knot have an even denser, and more absorbing, subarcsecond core, and was any [O III] 5007-Å emission from the host nebula on its near side? The densities and assumed temperatures of the globule cores derived from the CO emission (Huggins et al. 1992) appear to be consistent with pressure equilibrium between the ionized environment and the globule, so a globule with a cold dense core and an r^{-2} density gradient could be expected. The [O III] 5007-Å WFPC2 *HST* images of O'Dell & Handron (1996), with their 0.1-arcsec resolution, when combined with the present MES [O III] 5007-Å spectroscopy, now permit quantitative answers to both questions.

A 0.4-arcsec-wide cut through the dark core of Knot 1 from the *HST* [O III] 5007-Å image is shown in Fig. 14. This has been taken perpendicularly to the knot's long axis. It can be seen that the absorbing globule is 1.6-arcsec wide; also, its absorption is very flat-bottomed, which could imply saturation. However, the MES [O III] 5007-Å profiles over the knot's core are very similar to those for Knots 14 and 38 in Fig. 7 (and not shown hmere), i.e., the absorption is occurring in only the receding velocity component of the [O III] 5007-Å emission from the host nebula. The absorption zero

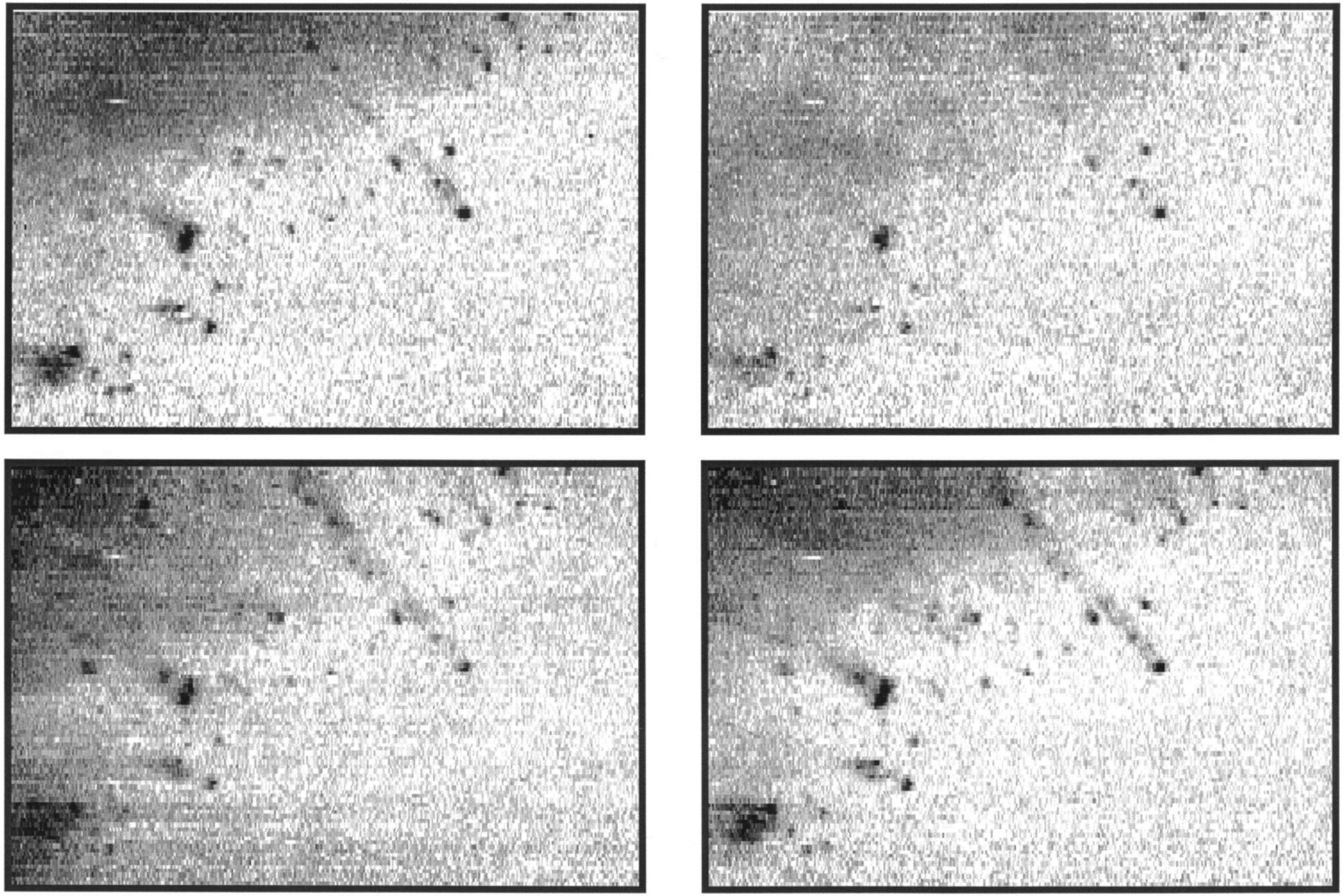

Figure 12. Velocity images in the light of [N II] 6584-Å of the head and tail of Knot 38 extracted from the stepped, multislit data array. The heliocentric radial velocity ranges for the four images are as follows: bottom left -31 to $-27\ \mathrm{km\ s^{-1}}$, bottom right -25 to $-21\ \mathrm{km\ s^{-1}}$, top left -20 to $-15\ \mathrm{km\ s^{-1}}$, and top right -14 to $-10\ \mathrm{km\ s^{-1}}$.

© 1998 RAS, MNRAS **294**, 201–223

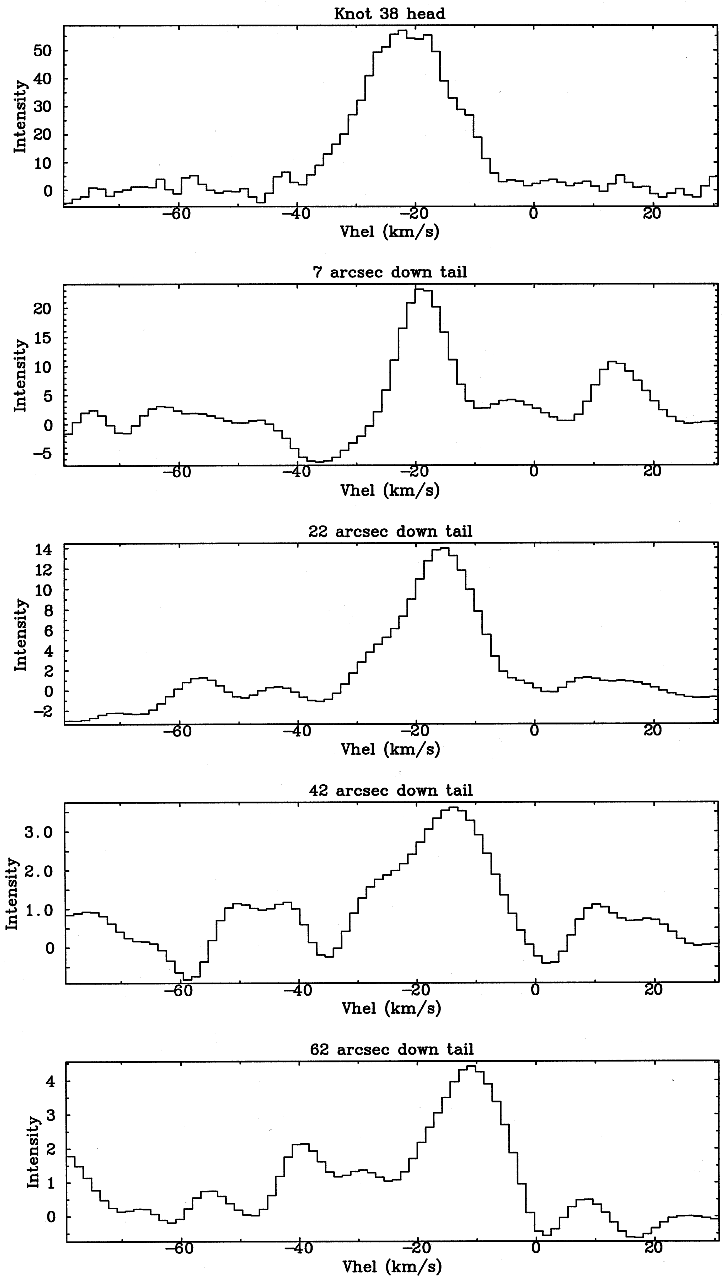

Figure 13. [N II] 6584-Å line profiles across the head and tail of Knot 38 extracted from a multislit data array.

marked in Fig. 14 then takes the foreground component of [O III] 5007 Å into account, as described for Knot 14 in Section 5.1.1. It is therefore concluded that the dusty, molecular core of Knot 1 transmits 30.5 per cent of the background [O III] 5007-Å emission, and has a uniform H_2 number density $n_g \approx 10^6\,cm^{-3}$ throughout its 1.6-arcsec diameter. This is comparable with the gas density from CO measurements given as $>10^5\,cm^{-3}$ by Huggins et al. (1992).

Some of the knots, including Knot 1, in the *HST* WFPC2 [O III] 5007-Å image (and in the previous NTT [O III] 5007-Å images; Meaburn et al. 1992) show definite absorption in their tails. This has now been measured for a cut 4 arcsec north of the core of Knot 1. The 1.8-arcsec-wide absorption feature is again very flat-bottomed and, again after correction for the near-side [O III] 5007-Å emission from the host nebula, transmits 79 per cent of the far side [O III] 5007-Å emission. A uniform density of H_2, $n_g \approx 4\times10^5\,cm^{-3}$, is implied.

6 DISCUSSION

6.1 Lifetimes of cometary knots

The ground-based Hα + [N II] 6584-Å images in Meaburn et al. (1992) showed about 600 emission knots around the

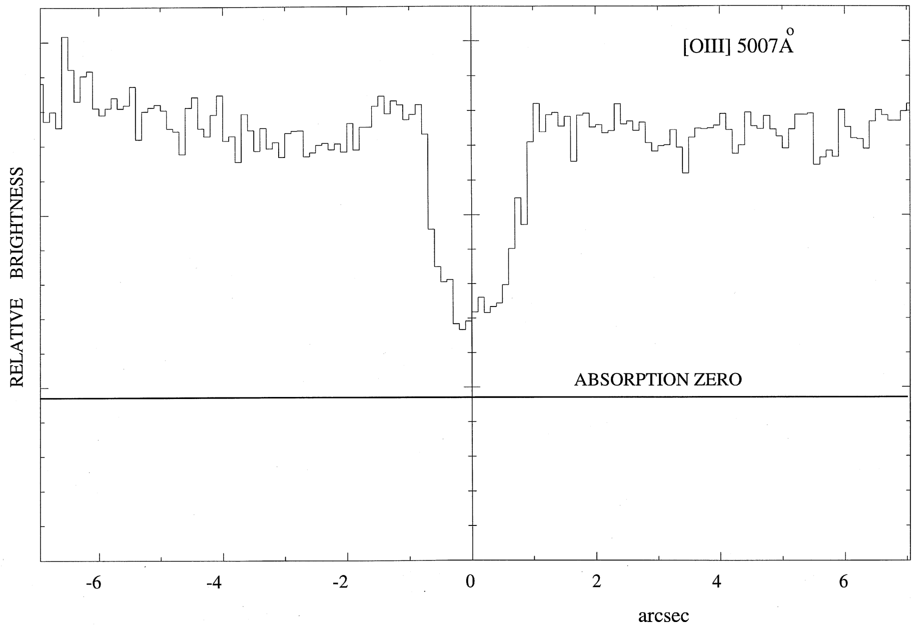

Figure 14. A cut, 0.4-arcsec wide, across the [O III] 5007-Å *HST* image of the centre of the dusty, molecular globule that forms the core of Knot 1. This cut is perpendicular to the globule's long-axis. The zero level for the absorption has been determined from an MES [O III] 5007-Å spectrum similar to those shown in Figs 10 and 11.

inner periphery of the bright ring of emission, whilst O'Dell & Handron (1996) counted some 300 in one WFPC2 frame. On the WFPC2 image the knots are all well resolved, implying sizes greater than 0.2 arcsec, and the largest knot has a diameter of ~ 3 arcsec. The knots therefore exist over a rather narrow range of sizes, and their morphological properties are remarkably similar. All display a narrow rim of [N II] 6584-Å emission, with Hα emission being more extended (both spatially and in velocity; see, e.g., Figs 7 and 8a–e). Only the knots closest to the central star show [O III] 5007-Å emission at their heads. Apart from a few cases (see, e.g., Fig. 6), knots at more positive velocities than the systemic radial velocity do not show strong absorption against the [O III] 5007-Å emission from the host nebula, whilst those at a more negative velocity show strong absorption. The kinematic structure of Knots 14 and 38 are remarkably similar, and examination of the global [N II] 6584-Å kinematics of the knots presented in Table 2 shows identical patterns. Thus, remarkably, the morphological and kinematic properties of all the knots are very similar.

Many of the knots in the various ground-based and *HST* [O III] 5007-Å images show definite absorption in their tails (see Section 5.3), suggesting that dust is being eroded from the globule. In this case, from the estimations of the globule and tail densities for Knot 1 in Section 5.3 the rate at which mass is being depleted from the globule can be derived. This then allows a limit on the globule lifetime to be predicted, assuming a constant velocity, time-independent, flow. Given a flow velocity of 10 km s^{-1} around the globule, a mass evaporation rate of 2.8×10^{-8} M$_\odot$ yr^{-1} is implied by the [O III] 5007-Å measurements of the tail of Knot 1 in Section 5.3. The mass of the globule, determined from its size and molecular density of 10^{-5} M$_\odot$ (Section 5.3), suggests that the globule would be completely eroded within only ≈ 500 yr. This is incompatible both with the kinematic age of the major ionized shells and the time taken for the globules to reach their present position (assuming ejection from the central star) at a constant velocity of ~ 14 km s^{-1} (Section 6.3), both of which indicate an age of at least ≈ 5000 yr. The very low turbulent motions (1–2 km s^{-1} would give expansion times of $\gg 1000$ yr) derived from CO measurements (Huggins et al. 1992) of the interior of the globules suggest that such erosion rather than expansion must be the dominant mechanism determining their lifetimes.

A more realistic model was therefore developed, in which the globule loses mass in the outer annulus orientated perpendicularly to the central star. The mass-loss of the globule by the ablating ionized gas is therefore proportional to the diameter of the globule (through the area of the annulus) and the difference in speeds of the neutral globule and the flow around the globule (taken here as ≈ 10 km s^{-1}; see Section 5.1.4). This material is dragged off into the tail. Some evidence for such a model is that the ratio of the mass-loss rate in the tail to the globule mass is similar, at 0.002 yr^{-1}, for two globules (Knot 1 and another knot to the NE) on the F502N image (chip 4). Given a mean density for the central globule of Knot 1 (taken as $n_g = 10^6$ cm^{-3}; see Section 5.3), only the original size of the globule (assumed spherical) and the width of the annulus are unknown variables. If the annulus remains fixed in width (a value of $\sim 10^{13}$ cm was found, which is consistent with the surface brightness of the line-emission regions around a globule), then the globule is eroded with a mass half-life of ~ 2400 yr. After 6000 yr the size of such a globule rapidly drops to zero in a few hundred years. Alternatively, if the thickness of the annulus depends on the globule radius, then the decay in size is almost linear with time. A suggestion that the annulus has a constant thickness is that it must be a mixing region governed by turbulent processes controlled primarily by the difference in velocity between the globule and the ionized gas. From the rather narrow range of globule sizes, as suggested by examination of the ground-based and WFPC2 [O III] 5007-Å images, a constant thickness for the ablation annulus is favoured. The limiting initial size of a globule to survive 6000 yr is 3.5 arcsec (2.2×10^{-3} pc); globules much smaller than this would have disappeared by the present time. Clearly, this is a simple model, but it does explain the salient features of the neutral globules and their tails. To test this model, it would be useful to study the morphology and relationship between the heads and tails of a larger sample of [O III] 5007-Å-absorbing globules.

6.2 The morphology and kinematics of the host nebula

It is now appropriate to discuss in more detail the spatio-kinematic relationship between the population of ionized knots and the main nebular structure. It is apparent from the above discussion that the knots occur in a region of space outside some minimum radius from the central star, but within that of the main [N II] 6584-Å shell. As argued in Meaburn et al. (1996), this region is toroidal in shape, since no knots are seen close to the central star.

An axially symmetric form for the main structure of the Helix nebula is generally preferred (see Section 1), and the toroidal region occupied by the knots would naturally be expected to have a common symmetry axis with the main structure, centred on the central star.

The sinusoidal distribution of the CO radial velocities (Healy & Huggins 1990; curve reproduced as the dashed line in Fig. 6) with PA for radii ≤ 300 arcsec suggests that this CO emission is arising in a relatively thin, expanding ring tilted to the plane of the sky along an axis at PA $=14°$ and with a maximum observed radial velocity component of ±19 km s^{-1}. Taylor (1977) observed the [O I] 6300-Å emissions from various points along the main limbs of the Helix nebula and found a velocity pattern strikingly similar to that observed by Healy & Huggins, although he interpreted this as arising from an extended helical structure. Taylor's observed radial velocities from this ring and the [N II] 6584-Å velocities of Meaburn & White (1982) are consistent with the CO velocities. Healy & Huggins (1990) suggested that much of the optical structure of the nebula is associated with ionization fronts on the surface of the molecular gas distribution, i.e., that the CO emission largely follows the [N II] 6584-Å emission. Meaburn & White (1982) suggested a bipolar structure for the main nebular shell, based on narrow-band [N II] 6584-Å images combined with kinematical information derived from Fabry–Perot interferograms. The $r \leq 300$ arcsec CO ring would thus correspond to the confining waist of the bipolar [N II] 6584-Å shell. This will be referred to as the equatorial ring; it is clearly visible as an elliptical structure, centred on the central star, in [N II] 6584-Å images of NGC 7293. The inclination of the plane of the equatorial ring to the plane of the sky is obtained from the dimensions of the observed ellipse to be $\theta = 37°$. The observed 19 km s^{-1} CO expansion velocity of this ring can thus be deprojected to give a true expansion velocity of ~ 31 km s^{-1}.

If the CO and [N II] 6584-Å rings are kinematically coupled, then the [N II] 6584-Å ring should show the same expansion velocity. A ring inclined at $\theta \sim 37°$ to the line of sight along an axis with PA $\sim 14°$ (from CO observations) intersects the EW axis at $r \sim \pm 242$ arcsec and the NS axis at $r \sim \pm 295$ arcsec. The pv arrays in Figs 5(a) and (b) show bright emission components at these positions, and corresponding (deprojected) velocities of 17, 17, 32 and 34 km s^{-1} (E, S, W and N respectively) can be derived, which are consistent with the CO result on the NW side but rather lower than the CO value on the SE side. This discrepancy may be partially accounted for by the inaccuracies in determining θ and the PA of the axis of tilt, estimated to add ± 6 km s^{-1} to each of these four derived expansion velocity values. The [N II] 6584-Å velocities will also contain components from localized flows around the base CO structures, as in the emission from the ionized knots.

The (axially symmetric) shape of the main CO/[N II] 6584-Å shell must take into account both the outer, bright [N II] 6584-Å limbs observed in images of the nebula, to the east and west of the ellipse corresponding to the equatorial ring, and also the fact that along the EW nebular cut (Fig. 5a) the observed velocity ellipse is incomplete, whereas along the NS cut (Fig. 5b) it is closed. It is also apparent from the EW cut that the outer E and W limbs (at $r \sim \pm 370$ arcsec) are observed to have low radial velocities. The simplest nebular structure to consider is a cylinder, with the outer E and W limbs being interpreted as the top and bottom rims of the cylinder. However, considering the $\theta = 37°$ angle of the symmetry axis to the line of sight, and the observed offset of the bright outer limbs along the symmetry axis of ~ 150 arcsec, there should be a clear line of sight through the centre of the nebula, whereas along both the EW and NS pv arrays (Figs 5a and b) two distinct faint components are observed from the central part of the nebula. It is also not clear why the outer rims of the cylinder should appear brightened in parts, to correspond with the observed outer limbs of the nebular structure. Meaburn & White (1982) proposed a closed, waisted, bipolar shape for the main [N II] 6584-Å emission region. As already discussed, the nebula cannot have a closed form, but an open-ended, waisted bipolar shape is consistent with the observed data. The bright outer limbs can be interpreted as limb-brightening of the lobes along the line of sight and the equatorial ring corresponds to the relatively dense waist of the shell. Such a shape is shown in Fig. 15. It was found that the dimensions of the lobes are quite tightly constrained by the observed spatial extents of emission seen in the EW and NS cuts through the nebula. The waisted bipolar shape also accounts for the material observed outside the ellipse corresponding to the equatorial ring, along the axis of tilt. The main kinematical features in the EW and NS cuts are also accounted for within this model; for example, one side of each lobe is observed more clearly than the other due to the limb-brightening effect. Where the limb-brightening is important, the lobes will be expanding roughly tangentially to the line of sight and therefore have low radial velocities; however, the opposite side of each lobe will appear to be much fainter, but is expanding outwards almost along the line of sight and therefore should show relatively high radial velocities. Indeed, this faint material is seen in Fig. 5(a) to have radial velocities of $\sim \pm 30$ km s^{-1} and, as the expansion here is close to the line-of-sight direction, this also

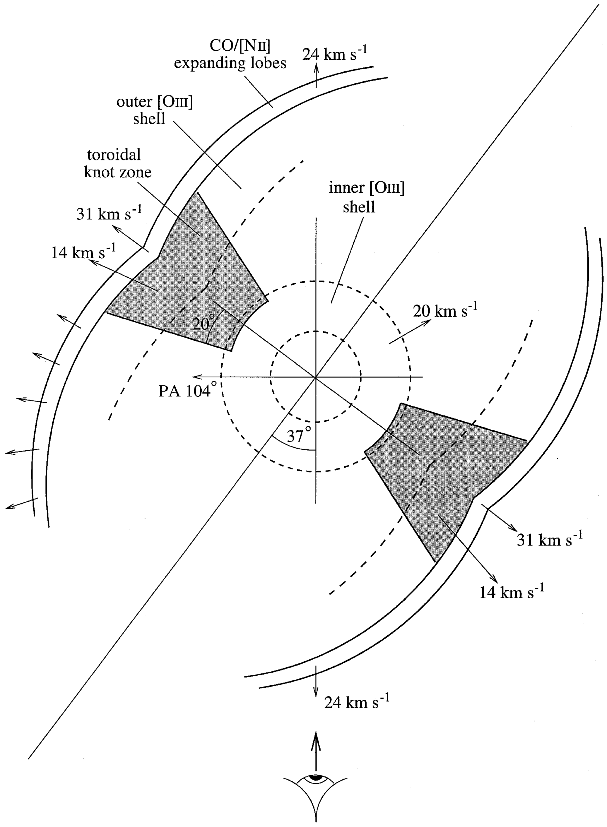

Figure 15. A schematic model of NGC 7293, in which many of the components are compared. The orientations, extents and relative positions of all of the components of NGC 7293 are best estimates from the various observations, and have been drawn to scale as far as possible. The knots are constrained within the shaded, toroidal zone on either side of the 'waist' of NGC 7293. The radial expansion of the system of knots is 14 km s^{-1} to be compared with the CO and [N II] 6584-Å expansion in the 'waist' of 31 km s^{-1}. The central [O III] 5007-Å-emitting shell is expanding at 20 km s^{-1}. The radial expansion velocity of 24 km s^{-1} observed along the line of sight through the central star is also indicated. The arrows on the upper left-hand lobe indicate the expected direction of expansion, which may contain a component along the lobe surface as well as a tangential component. This part of the lobe will appear limb-brightened to the observer and show a low radial expansion velocity. The inclination angle of the symmetry axis of the main nebular structure and the opening angle which defines the zone occupied by the cometary knots are also indicated.

implies that (given the assumption that expansion velocity increases with radius from the central star) the lobes are not highly elongated. The model also accounts quite neatly for the kinematical behaviour observed in the CO (Healy & Huggins 1990, their fig. 6) and [O I] 6300-Å (see plate 1 in Taylor 1977) observations, for the regions not covered by the equatorial ring. In both cases, the observed velocities tend towards the systemic along the positions of the two outer limbs.

There is some evidence from hydrodynamical simulations (Frank, Balick & Livio 1996) that when a fast stellar wind sweeps up a slow, preceding wind, the resulting bubble, if asymmetric, can exhibit a component of flow tangential to the bubble surface rather than purely normal pressure expansion. In an elongated, prolate structure, this flow converges into a relatively fast outflow at the poles, which may have blown open the main shell of the nebula earlier in its evolution. The presence of the faint, extended material to the SE and NW of the main [N II] 6584-Å shell could then be accounted for by relatively high-velocity material escaping from the shell. The observed radial expansion of ± 24 km s^{-1} along the line of sight through the central star, reported in Meaburn et al. (1996), must now be interpreted as a lower limit to the true expansion velocity of the lobes. In fact, since the density of the expanding bipolar shell would be expected to decrease with distance from the central star and therefore the expansion velocity would be expected to increase accordingly, the lobes are probably expanding at ≥ 31 km s^{-1}, the expansion velocity of the equatorial ring.

The inner part of the nebula was shown by Meaburn & White (1982) to contain complex [O III] 5007-Å structures. They proposed an inner, spherical shell of [O III] 5007 Å, expanding at ~ 20 km s^{-1}, and an outer shell located just within and following the bipolar shape of the [N II] 6584-Å emission. This outer shell is thought to be an ionization stratification effect within the main nebular shell, i.e., the [O III] 5007-Å shell is the inner surface of the main CO/[N II] 6584-Å shell.

6.3 Relationship of knots and host nebula

Having established a plausible form for the main low- and high-ionization structures, the system of cometary knots is now considered. As previously noted, the knots probably have a toroidal distribution, in the same plane as the equatorial ring. Knot 14 is at an observed radius of 128 arcsec from the central star and appears, in projection, to lie along the axis of tilt of the main nebular shell; however, since the tail is believed to project out of the plane of the sky (at an angle of 25°; see Table 3), the knot must lie above the equatorial plane. From geometrical arguments, this leads to a true radial distance of 141 arcsec. Knot 38 appears to be closest to the central star, at an observed radius ≥ 95 arcsec. This corresponds to a lower limit of 111 arcsec for the deprojected radius, taking the lower limit of 32° for the angle of the knot's tail to the plane of the sky (Section 5.2), which is taken as a lower limit to the inner radius of the knot distribution. This is roughly coincidental with the outer limit of the inner [O III] 5007-Å shell. The toroidal region containing the knots is here assumed to be defined in the radial direction to lie between this minimum radius and the main nebular shell, and confined to within an opening angle α measured from the equatorial plane, as shown in Fig. 15. An estimate of the opening angle can be obtained from the position of Knot 14 to be 20°, making the assumption that this knot lies on the outer edge of the distribution. If $\alpha = 20°$ and $r_{min} = 95$ arcsec are taken as defining the zone within which the knots are found, then a clear zone of ± 32 arcsec along the projected symmetry axis (i.e., PA = 104°) would be expected, which is well within the observed knot-free zone.

The global expansion velocity of the system of knots, observed to be $V_{KNOTS} \sim 11.4$ km s^{-1} (Fig. 6) deprojects to give a true value of ~ 14 km s^{-1}. The toroidal distribution pattern will naturally give rise to the spread of velocities as a function of PA about the sinusoidal curve defined by knots lying in the equatorial plane (see Fig. 6). The knots are then being overrun not by the central [O III] 5007-Å-emitting shell but by the [O III] 5007-Å-emitting zone on the inside of the CO and [N II] 6584-Å ring expanding at 31 km s^{-1}. This model still also accounts for the fact that most of the western knots are [O III] 5007-Å-absorbing (i.e., near-side), although they can appear as non-absorbing (far-side) provided they are observed through this outer [O III] 5007-Å shell. This line-of-sight effect means that apparent far-side knots can even have approaching radial velocities.

Cox (1997, private communication) and Young et al. (1997) report the discovery of molecular globules in the more diffuse molecular material of the outer CO rings. They suggest that these have similar sizes and densities to the molecular cores of the ionized knots discussed here, in which case, if this population of outer globules has also a similar global expansion velocity as the outer CO shell, some doubt will be cast on the present interpretation of the inner, exposed, knots as being overrun by the outer shell. An alternative model, however, would have to explain the limited range of knot radial velocities in Fig. 6 and the presence of elongated, dusty tails.

6.4 Conclusions

A comprehensive observational study of the cometary knots in the Helix planetary nebula (NGC 7293) has been described. Imaging in [O III] 5007 Å and Hα + [N II] 6584 Å has revealed the detailed emission and absorption structure, and a remarkable uniformity in properties of the knot (and the core globule) population. The kinematics of 50 knots have been revealed both by line-fitting of their profiles and by generating emission-velocity cubes built up from many multislit exposures. The population of knots has a systematically lower expansion velocity than the large-scale ionized gas, which has also been studied by two orthogonal lines of long-slit velocity measurements. The kinematics of two knots have been studied in detail in emission lines from ions with a range of ionizing energies, complementing CO data. A picture of dense neutral globules with mildly supersonic flows of ionized gas (i.e., the knots and tails) around their peripheries is revealed with the expanding ionized gas of the host nebula sweeping past them. The estimated erosion rate of the globules is consistent with only the larger globules now being observable.

The large-scale structure of the Helix nebula can be best matched by a bipolar structure, with the cometary knots situated in a thick equatorial ring. Whilst the data do not unequivocally distinguish between the various theories for the origin of the knots, it appears most probable that they are the remnants of the higher density, dusty, red giant wind. They are then being overrun and eroded, not directly by a hot, fast wind, but by the subsequent swept-up CO/[N II] 6584-Å nebular shell.

ACKNOWLEDGMENTS

We acknowledge the excellent assistance of staffs at the Anglo-Australian, Isaac Newton and New Technology (ESO) telescopes where these observations were made. The authors acknowledge the data analysis facilities provided by the Starlink Project, which is run by CCLRC on behalf of PPARC.

REFERENCES

Acker A., 1978, A&AS, 33, 367
Bohlin R. C., Savage B. D., Drake J. E., 1978, ApJ, 224, 132
Bohlin R. C., Harrington J. P., Stecher T. P., 1982, ApJ, 252, 635
Cahn J. H., Kaler J.B., 1971, ApJS, 22, 319
Cahn J. H., Kaler J. B., Stanghellini L., 1992, A&AS, 94, 399
Capriotti E. R., 1973, ApJ, 179, 495
Clayton C. A., 1987, A&A, 173, 137
Daub C. T., 1982, ApJ, 260, 612
Dyson J.E., Hartquist T. W., Pettini M., Smith L. J., 1989, MNRAS, 241, 625
Dyson J. E., Hartquist T. W., Biro S., 1993, MNRAS, 261, 430
Forveille T., Huggins P. J., 1991, A&A, 248, 599
Frank A., Balick B., Livio M., 1996, ApJ, 471, L53
Hartquist T. W., Dyson J. E., 1993, QJRAS, 34, 57
Healy A. P., Huggins P. J., 1990, AJ, 100, 511
Hildebrandt R. H., 1983, QJRAS, 24, 267
Huggins P. J., Healy A. P., 1986, ApJ, 305, L29
Huggins P. J., Bachiller R., Cox P., Forveille T., 1992, ApJ, 401, L43
Kastner J. H., Weintraud D. A., Gatley I., Merrill K. M., Probst R. G., 1996, ApJ, 462, 777
Kirkpatrick J. P., 1972, ApJ, 176, 381
Meaburn J., White N. J., 1982, Ap&SS, 82, 423
Meaburn J., Blundell B., Carling R., Gregory D. F., Keir D., Wynne C., 1984, MNRAS, 210, 463
Meaburn J., Walsh J. R., Clegg R. E. S., Walton N. A., Taylor D., Berry D. S., 1992, MNRAS, 255, 177
Meaburn J., Clayton C. A., Bryce M., Walsh J. R., 1996, MNRAS, 281, L57
O'Dell C. R., Handron K. D., 1996, AJ, 111, 1630
Steffen W., Holloway A. J., Pedlar A., 1996, MNRAS, 282, 1203
Storey J. W. V., 1984, MNRAS, 206, 512
Taylor K., 1977, MNRAS, 181, 475
Terrett D. L., 1979, MNRAS, 186, 127
Van Blerkom D., Arny T., 1972, MNRAS, 156, 91
Vishniac E. T., 1994, ApJ, 428, 186
Vorontsov-Velyaminov B.A., 1968, in Osterbrock D. E., O'Dell C. R., eds, Proc. IAU Symp. 34, Planetary Nebulae. Reidel, Dordrecht, p. 256
Walsh J. R., Meaburn J., 1987, MNRAS, 224, 885
Walsh J. R., Meaburn J., 1993, Messenger, 73, 35
Warner J. W., Rubin V. C., 1975, ApJ, 198, 593
Young K., Cox P., Huggins P. J., Forveille T., Bachiller R., 1997, ApJ, 482, L101